



HAL
open science

Intrinsic precursors and timescale of the tropical Indian Ocean Dipole: insights from partially decoupled numerical experiment

Julien Crétat, Pascal Terray, Sébastien Masson, K. P. Sooraj

► To cite this version:

Julien Crétat, Pascal Terray, Sébastien Masson, K. P. Sooraj. Intrinsic precursors and timescale of the tropical Indian Ocean Dipole: insights from partially decoupled numerical experiment. *Climate Dynamics*, 2018, 51 (4), pp.1311-1332. 10.1007/s00382-017-3956-7. hal-01673448

HAL Id: hal-01673448

<https://hal.science/hal-01673448>

Submitted on 29 Dec 2017

HAL is a multi-disciplinary open access archive for the deposit and dissemination of scientific research documents, whether they are published or not. The documents may come from teaching and research institutions in France or abroad, or from public or private research centers.

L'archive ouverte pluridisciplinaire **HAL**, est destinée au dépôt et à la diffusion de documents scientifiques de niveau recherche, publiés ou non, émanant des établissements d'enseignement et de recherche français ou étrangers, des laboratoires publics ou privés.

25 **Abstract**

26

27 The intrinsic precursors and timescale of the tropical Indian Ocean Dipole (IOD) are
28 examined with the help of a partially coupled global experiment with decoupled SST over the
29 tropical Pacific.

30

31 The IOD does exist in the absence of El Niño Southern Oscillation (ENSO) in our modeling
32 framework, but has weaker amplitude and damped Bjerknes feedback. However, IOD
33 variability is much more biennial in the absence than presence of ENSO, especially in the
34 eastern equatorial Indian Ocean (IO). Such biennial rhythm results mainly from two
35 mechanisms internal to the IO.

36

37 The tropical ocean dynamics play a key role in the biennial anomalies during boreal winter
38 with a sudden reversal of thermocline anomalies in the eastern equatorial IO forced by
39 intraseasonal disturbances reminiscent of the Madden-Julian Oscillation (MJO). Such
40 preconditioning is stronger after the occurrence of negative IOD events during the preceding
41 boreal fall, underlying two-way interactions between IOD and MJO and asymmetry in this
42 relationship. However, this preconditioning is not sufficient for triggering IOD events in the
43 next boreal spring *per se*.

44

45 The main trigger for pure IODs relates to tropical-extratropical interactions within the IO,
46 Convection and diabating heating associated with negative IODs promote a Gill-type tropical
47 response, excite mid-latitude wave-trains and subtropical blocking in the Southern
48 Hemisphere that trigger positive subtropical IOD events during boreal winter. The latter

49 promotes cold SST and anticyclonic circulation anomalies over the southeast IO that persist
50 and migrate northeastward, triggering positive IOD events during the next boreal spring.

51

52 Accounting for the complementary influence of tropical ocean dynamics coupled to MJO and
53 tropical-extratropical ocean-atmosphere interactions may thus help improving IOD
54 predictability.

55

56

57 **Keywords:** biennial variability – coupled climate model – Indian Ocean Dipole – MJO –
58 ocean dynamics – tropical-extratropical interactions

59

60

61 **1. Introduction**

62

63 The Indian Ocean Dipole (IOD) is an important ocean–atmosphere coupled mode of
64 variability in the Indian Ocean (IO; Saji et al. 1999; Webster et al. 1999; Schott et al. 2009).
65 Positive IOD events (pIODs) are associated with cool SST and shallow thermocline in the
66 eastern IO, and warm SST and deep thermocline in its western part. The reverse holds for
67 negative IOD events (nIODs). The IOD typically initiates during boreal spring and peaks in
68 September–November (SON) in relation to wind–thermocline–Sea Surface Temperature
69 (SST) and wind–evaporation–SST feedbacks (Annamalai et al. 2003; Li et al. 2003; Fischer et
70 al. 2005; Spencer et al. 2005; Terray et al. 2007; Schott et al. 2009; Wang and Wang 2014).
71 The former feedback known as the Bjerknes feedback, materializes positive coupled
72 interactions between zonal wind, SST and thermocline anomalies over the equatorial IO
73 during boreal fall and plays a central role in the IOD amplitude and length in both
74 observations and current coupled models (Schott et al. 2009; Liu et al. 2014). The IOD
75 significantly modulates rainfall interannual variability of surrounding (e.g., Ashok et al. 2003;
76 Black et al. 2003; Gadgil et al. 2004; Behera et al. 2005; Ummenhofer et al. 2009;
77 Krishnaswamy et al. 2015) and remote (e.g., Saji and Yamagata 2003; Yamagata et al. 2004;
78 Chan et al. 2008; Cai et al. 2011) regions. Predicting IOD is thus of primary importance for
79 improving our ability in seasonal rainfall forecasting. However, IOD prediction skill remains
80 very limited and much shorter than the one associated with El Niño Southern Oscillation
81 (ENSO, Shi et al. 2012; Liu et al. 2016).

82

83 Developing El Niños frequently trigger pIODs by inducing subsidence in the eastern
84 equatorial IO, low-level anticyclonic circulation over the southeastern IO and upwelling-
85 favorable winds off Java–Sumatra (Annamalai et al. 2003; Gualdi et al. 2003; Shinoda et al.

86 2004a-b; Fischer et al. 2005; Yu and Lau 2005; Behera et al. 2006; Schott et al. 2009; Hong et
87 al. 2010; Guo et al. 2015). This scenario reverses during developing La Niñas and stands for
88 most ENSO events, except some ENSO Modoki events (Wang and Wang 2014). Guo et al.
89 (2015) have suggested that the IO basinwide mode induced by ENSO (Klein et al. 1999; Lau
90 and Nath 2003; Schott et al. 2009) might also influence on IOD variability through generation
91 of anomalous off-equatorial ocean Rossby waves and their effects on the western IO (Schott
92 et al. 2009).

93
94 Many additional tropical mechanisms have also been proposed as potential triggers for IOD
95 (Kajikawa et al. 2003; Fischer et al. 2005; Drbohlav et al. 2007; Yan and Liu 2009; Guo et al.
96 2013, 2015; Sun et al. 2015; Wang et al. 2016). Meehl et al. (2003), Drbohlav et al. (2007)
97 and Sun et al. (2015) underline the role of the Indian Summer Monsoon (ISM) circulation in
98 warming the western IO and cooling the eastern tropical IO during boreal summer. Another
99 potential trigger for IOD involves boreal spring convection over Indonesia and the western
100 Pacific (Kajikawa et al. 2003; Hendon 2003; Wang et al. 2016), with above (below) than
101 normal convection driving westerly (easterly) wind anomalies over the equatorial IO that
102 trigger nIODs (pIODs). Yan and Liu (2009) also suggest that the intra-seasonal atmospheric
103 forcing such as, the Madden–Julian oscillation (MJO), plays a significant role in IOD
104 triggering. In addition, the relationships between the Indonesian Throughflow, IOD and
105 ENSO have also been highlighted (Tozuka et al. 2007; Yuan et al. 2011; Sprintall and
106 Revelard 2014).

107
108 The extratropical IO is another important potential trigger for IOD (Terray et al. 2005, 2007;
109 Fischer et al. 2005; Guo et al. 2015). Pure IODs can be triggered by anomalous winds along
110 the Java-Sumatra coast (Fischer et al. 2005; Guo et al. 2015). These southeasterly winds relate

111 to intensification of the Mascarene High (Terray et al. 2005) that force the so-called
112 Subtropical IO Dipole (SIOD) during the previous boreal winter and spring (Behera and
113 Yamagata 2001; Suzuki et al. 2004; Morioka et al. 2012). During its positive phase, the cold
114 SST anomalies in the eastern SIOD pole favor a regional anticyclonic anomalous circulation
115 and upwelling-favorable winds off Java-Sumatra (Fischer et al. 2005; Terray et al. 2007).

116

117 In addition, oceanic dynamics within the IO have been shown to be critical for IOD triggering
118 and termination (Murtugudde et al. 2000; Feng and Meyers 2003; Shinoda et al. 2004b; Rao
119 and Behera 2005; Rao et al. 2009; McPhaden and Nagura 2014). IOD variability depicts
120 many features of the delayed oscillator theory (Webster et al. 1999; Murtugudde et al. 2000;
121 Feng and Meyers 2003; Yamagata et al. 2004; Rao and Behera 2005; Yuan and Liu 2009;
122 Wang and Yuan 2015) and recharge oscillator theory (McPhaden and Nagura 2014)
123 traditionally developed for understanding ENSO (Battisti and Hirst 1989; Jin 1997). This
124 implies that wind-forced oceanic waves in the IO and their western and eastern boundary
125 reflections are important to predict the surface dipole independently from ENSO (Wang and
126 Yuan 2015; McPhaden and Nagura 2014; Delman et al. 2016). Boreal spring anomalous
127 anticyclonic circulation off Java-Sumatra forces equatorial upwelling Kelvin waves, which
128 are essential for SST cooling along Java and pIOD triggering during boreal spring (Delman et
129 al. 2016). Such anomalous atmospheric circulation also generates equatorial and off-
130 equatorial downwelling Rossby waves, which can reflect at the western boundary of the IO
131 into downwelling equatorial Kelvin waves, helping terminating pIODs and promoting
132 favorable conditions for nIOD development during the following year (Rao et al. 2002, 2005;
133 Feng and Meyers 2003; Yuan and Liu 2009).

134

135 This review illustrates that IOD can be triggered by a large variety of local and remote

136 phenomena. The extent to which many of these IOD precursors are independent of ENSO is,
137 however, hardly quantifiable in most studies since they make use of observations or models
138 that contain ENSO variability. Recently, Stuecker et al. (2017) argue that IOD and its biennial
139 timescale can be fully explained by ENSO and the seasonal modulation of ocean-atmosphere
140 feedbacks over the Indo-Pacific region without any significant ocean memory in the IO, thus
141 reactivating the old debate on the nature of IOD variability (Schott et al. 2009). A way to
142 clarify the intrinsic IOD predictors and timescale (e.g., biennial variability), without any
143 interference with ENSO, is using coupled ocean-atmosphere simulations with partial
144 decoupling over the tropical Pacific to forbid ENSO development and variability. Such
145 approach has been successfully used for analyzing the roles of Indian and Atlantic Oceans on
146 ENSO (Luo et al. 2010; Santoso et al. 2012; Terray et al. 2016; Kajtar et al. 2016), the impact
147 of SST errors on ISM (Prodhomme et al. 2014), the two-way relationship between IOD and
148 ISM (Crétat et al. 2016), and the IOD and its forcing mechanisms in the absence of ENSO
149 (Fischer et al. 2005; Behera et al. 2006; Yang et al. 2015; Wang et al. 2016; Stuecker et al.
150 2017). Here, this methodology is used to re-examine intrinsic IOD precursors and timescale,
151 if any, in the absence of ENSO.

152

153 The paper is organized as follows. Section 2 presents the observations, the model
154 experiments, and the methodology used. Section 3 is model validation and discusses the basic
155 effects of ENSO removing on IOD during its peak and the associated Bjerknes feedback.
156 Section 4 identifies the main precursors for IOD in both the presence and absence of ENSO.
157 Section 5 focuses on the IOD timescale in the absence of ENSO, including the role of ocean
158 dynamics, MJO and tropical-extratropical interactions in preconditioning and triggering pure
159 IODs. Section 6 gives main conclusions and discussion.

160

161

162 **2. Data and method**

163

164 *2.1) Experimental setup*

165

166 Two global simulations are run using the SINTEX-F2 model (Masson et al. 2012) with the
167 ECHAM5.3 atmosphere (Roeckner et al. 2003) at T106 spectral resolution ($\sim 1.125^\circ \times 1.125^\circ$)
168 and 31 hybrid sigma-pressure levels, and the NEMO ocean (Madec 2008) at $0.5^\circ \times 0.5^\circ$
169 horizontal resolution, 31 vertical levels and with the LIM2 ice model (Timmermann et al.
170 2005). The two model components are coupled using the Ocean–Atmosphere–Sea–Ice–Soil
171 (OASIS3) coupler (Valcke 2006). The coupling information is exchanged every 2h. The
172 model does not require flux adjustment to maintain a near stable climate, and accurately
173 simulates the tropical Pacific SST mean state, ENSO variability, and the monsoon–IOD–
174 ENSO relationships (Masson et al. 2012; Terray et al. 2012, 2016; Cr  tat et al. 2016). It is
175 also a state-of-the-art tool to forecast tropical variability (Doi et al. 2016).

176

177 A 210-yr fully coupled ocean-atmosphere simulation is used as a control (CTL hereafter). The
178 CTL is compared to a 110-yr partially coupled simulation similar to CTL, except over the
179 tropical Pacific (30°S – 30°N band, see Fig. 1h in Cr  tat et al. 2016) where SST is nudged
180 toward the CTL daily climatology. This partially coupled simulation will be called FTFC here
181 and after. Following Luo et al. (2005), the nudging method used in the FTFC modifies the
182 non-solar heat fluxes in the tropical Pacific Ocean through a correction term, scaling with the
183 SST model error, that completely removes ENSO-scale variability without affecting the
184 physical consistency between SST and ocean dynamics in the nudged domain (Prodhomme et
185 al. 2015; Terray et al. 2016). The damping term in this nudging technique ($-2400 \text{ W m}^{-2} \text{ K}^{-1}$)

186 corresponds to the 1-day relaxation time for temperature in a 50-m ocean layer. The first 10
187 years of both simulations are excluded to let the model spin-ups.

188

189 *2.2) Observations and reanalyses*

190

191 Multiple data sources are used for model validation. SST are taken from the 1° x 1° Hadley
192 Centre Sea Ice and Sea Surface Temperature dataset V1.1 (HadISST; Rayner et al. 2003)
193 available from 1870 onwards. The depth of the 20°C isotherm (20D) is used as a proxy for
194 thermocline depth and is computed using the ocean temperature profiles from the SODA
195 V2.2.4 reanalysis (Giese and Ray 2011), available for 1871–2008 at the 0.5° x 0.5° horizontal
196 resolution and 40 vertical levels. The SODA V2.2.4 wind stress, which is derived from the
197 NOAA 20th Century Reanalysis (Compo et al. 2011), is also used for estimating the Bjerknes
198 feedback associated with IOD during its peak season in Section 3.2. Since SODA produces its
199 own SST physically consistent with the 20D and wind stress time series used here, this
200 alternate SST dataset has been used to assess the robustness of the strength in the observed
201 Bjerknes feedback in Section 2.3. However, this different SST dataset show similar results, so
202 we only present here the results with HadISST SST in this study. Large-scale atmospheric
203 circulation, including 10-m and 850-hPa winds and 200-hPa velocity potential, is provided by
204 the 1.5° x 1.5° ECMWF ERA-Interim reanalysis (ERA-I; Dee et al. 2011) available from
205 1979 onwards. All these quantities are interpolated onto the model resolution to foster direct
206 comparison with the CTL and FTFC and analyzed for the 1979–2008 period since ERA-I
207 starts in 1979 and SODA data ends in 2008.

208

209 *2.3) Methods*

210

211 The IOD index is first defined as the SST anomaly gradient between the western equatorial

212 IO (50°–70°E, 10°S–10°N) and the southeastern equatorial IO (90°–110°E, 10°S–Eq)
213 following Saji et al. (1999), and is used as a baseline for discussing a refined Bjerknes
214 feedback definition of the IOD based on a multivariate technique accounting for the IOD
215 pattern distortion in current coupled models (Cai and Cowan 2013; Terray et al. 2012; Crétat
216 et al. 2016).

217
218 The strength of the Bjerknes feedback is defined using a singular value decomposition
219 technique (Wallace et al. 1990; Bretherton et al. 1992) applied to the covariance matrix
220 between all couplets of SST, 20D and wind stress (USTR) monthly anomalies in the 10°S–
221 10°N band during boreal fall (i.e., SON). This approach, called Maximum Covariance
222 Analysis (MCA), has been demonstrated to be more efficient than simple regression method
223 based on area-averaged time series for studying the Bjerknes feedback in the tropical Pacific
224 (Masson et al. 2012; Terray et al. 2016). The MCA between two fields extracts modes of
225 spatio-temporal co-variability ranked according to their square covariance fraction (SCF). For
226 each mode, each field is characterized by an expansion coefficient (EC) time series and an
227 associated spatial pattern. The regression map between one field and its EC time series, the
228 so-called “homogenous vector”, gives its spatial pattern. The first mode of the three MCAs
229 (between each pair of variables in the set of SST, 20D and wind stress) only is analyzed here
230 because it documents each branch of the IOD-related Bjerknes feedback and explains most of
231 the co-variability between the different couplets in both observations and simulations. The
232 strength of this feedback is assessed using the correlation value (r) between the EC time series
233 of the two fields and the normalized root-mean-square covariance (NC; Zhang et al. 1998)
234 measuring how strongly related the coupled patterns are. The relationship between the
235 Bjerknes feedback and IOD is also assessed by correlating each EC time series to the Saji’s
236 IOD index to test the robustness of our approach.

237

238 The IOD precursors and their associated mechanisms are finally examined through regression
239 analyses. The statistical confidence of these regressions is evaluated by comparing the slope
240 of each regression to the 90th percentile threshold value derived from 1000 regressions with
241 randomly permuted regressor having mean and variance similar to the original regressor.

242

243

244 **3. Effects of ENSO on boreal fall IOD patterns and associated Bjerknes feedback**

245

246 This section evaluates the model ability in simulating boreal fall IOD pattern/amplitude and
247 associated Bjerknes feedback and assesses the extent to which these characteristics are
248 influenced by ENSO.

249

250 **3.1 Boreal fall IOD pattern and amplitude**

251

252 The standard deviations of the Saji's IOD index during SON are 0.39, 0.48, and 0.35 K for the
253 observations and the CTL and FTFC experiments, respectively. This suggests IOD does still
254 exist without ENSO as an intrinsic mode of variability, but with slight reduction in amplitude,
255 consistent with previous studies (Fischer et al. 2005; Behera et al. 2006; Luo et al. 2010;
256 Santoso et al. 2012; Sun et al. 2015; Wang et al. 2016; Crétat et al. 2016). The observed
257 seasonal phase-locking of IOD is also well reproduced by the CTL and FTFC experiments
258 (not shown; see Crétat et al. 2016). The regression maps of the climate anomalies related to
259 the IOD during its peak season (e.g., boreal fall) are shown in Fig. 1. In the observations,
260 pIODs oppose cool SST, shallow thermocline and below-than-normal rainfall anomalies in
261 the eastern equatorial IO to reversed anomalies further west and these equatorial SST and
262 rainfall gradients are well correlated to the equatorial easterly zonal wind anomalies over the

263 central IO (Fig. 1a-b). The SST and 20D anomalous patterns are more tightly coupled in the
264 eastern equatorial than western tropical IO, consistent with previous studies (Xie et al. 2002;
265 Schott et al. 2009).

266

267 The IOD pattern is very similar between the two experiments and captures the main observed
268 features (Fig. 1c-f). The two experiments largely overestimate the spatial coverage of cool
269 SST and negative 20D anomalies in the eastern IO, especially along the equator (Fig. 1c-d)
270 due to exaggerated boreal fall upwelling in the SINTEX and other models (Fischer et al.
271 2005; Cai et al. 2009; Liu et al 2014). Also, SST warming and its coupling with rainfall are
272 underestimated over the western and southwestern IO regions where the simulated
273 thermocline is too deep all year long (not shown). These common errors suggest that a large
274 part of the model IOD biases may have a local origin internal to the IO or, at least, that these
275 errors are not linked to deficiencies in the simulation of ENSO in our coupled model.

276

277 3.2 IOD and Bjerknes feedback

278

279 The Bjerknes feedback is examined during the IOD peak season based on the summary
280 statistics for the first mode of the three MCAs (see Section 2.3), shown in Tables 1-3, and the
281 homogeneous maps (Fig. 2). These three MCA1s account for most of the SST–20D, SST–
282 USTR and 20D–USTR co-variability during SON in both the observations and the model,
283 with SFC ranging from 79% up to 97% depending on both the couplet and data considered
284 (Tables 1-3; column 1). Furthermore, the EC time series and homogeneous maps of SST
285 derived from both the SST–20D and SST–USTR couplets are similar, with temporal and
286 spatial correlations above +0.99 for both the observations and the simulations (not shown).
287 This is why the SST variance described by MCA1 is almost equal in the SST–USTR and

288 SST–20D couplets (Tables 1-2; column 4). Such similarity also stands for 20D (Tables 2-3;
289 columns 4-5, respectively) and USTR (Tables 1,3; column 5). Therefore, the three MCA1s
290 depict different facets of a unique ocean-atmosphere coupled mode of co-variability, the
291 Bjerknes feedback, which explains most of the ocean-atmosphere co-variability during boreal
292 fall. The patterns of this coupled mode (Fig. 2) clearly resemble the Saji’s IOD patterns (Fig.
293 1), with east-west asymmetry in SST and 20D in the equatorial IO (Fig. 2a-f) coupled to
294 strong easterly USTR anomalies over the central tropical IO (Fig. 2g-i). However, the USTR
295 anomalous pattern is symmetrical about the equator in the two simulations and resembles to a
296 Gill-type atmospheric response to convection anomalies over the eastern equatorial IO and
297 Maritime Continent (Schott et al. 2009). On the other hand, the observed SST and USTR
298 patterns are much more asymmetrical. This suggests that observed SST variability over the
299 southeast IO modulates atmospheric convection and drives a strong asymmetrical atmospheric
300 Rossby wave response to its west (Li et al. 2003). Despite these differences, the eastern IO
301 dominates the co-variability between SST, USTR and 20D during SON in both observations
302 and simulations. The year-to-year variability of this coupled mode is also phased to that of the
303 Saji’s IOD definition since the latter is highly and positively correlated with the different EC
304 time series (Tables 1-3; columns 6-7, respectively). Thus, variability of the EC time series
305 explains well the amplitude of the IOD as viewed from the strength of the Bjerknes feedback.

306

307 This confirms the key-role of the positive Bjerknes feedback during the mature phase of
308 observed and simulated IODs (e.g., Li et al. 2003; Fischer et al. 2005; Spencer et al. 2005;
309 Schott et al. 2009). Some differences are, however, noticeable between the observations and
310 the model. Despite exaggerated IOD amplitude in the model, the correlations between the
311 Saji’s IOD index and the EC time series are systematically greater in the observations,
312 especially for the different 20D EC time series (Tables 2-3; column 6). This difference is

313 fairly reduced when removing the 5°S–5°N band in the western IO box prior to compute the
314 Saji’s IOD index in the model (column 7 in Tables 1-3). The use of the Bjerknes-oriented
315 IOD definition allows taking into account such pattern distortion in the model (Fig. 1) and
316 illustrates the benefits of our MCA approach.

317

318 The strength of the Bjerknes feedback may be quantified by the SFC, NC and r statistics in
319 each MCA (see Section 2.3). The SFC, NC and r values between the EC time series of the left
320 and right fields are strong whatever the couplet and data considered (Tables 1-3; columns 1-3,
321 respectively). However, some differences are again noticeable between the observations and
322 the model. First, the hierarchy in the coupling strength is metric dependent in the
323 observations, while robust across the different metrics in the model, with the SST–20D and
324 SST–USTR couplings systematically ranked first and last, respectively. The model also
325 exaggerates the strength of the SST–20D and USTR–20D couplings, even in the absence of
326 ENSO. Once again, this model bias relates to too shallow thermocline over the eastern
327 equatorial IO (not shown) that exacerbates both the thermocline response to the wind forcing
328 and the SST response to the thermocline forcing (Figs. 1c,e and 2b-c).

329

330 Removing ENSO slightly but significantly weakens the IOD-related Bjerknes feedback, as
331 reflected by systematic lower statistical scores for the FTPC than the CTL (Tables 1-3;
332 columns 1-3, respectively). While a large fraction of the positive Bjerknes feedback is linked
333 to ocean-atmosphere interaction internal to the IO, in accordance with Fischer et al. (2005)
334 and Behera et al. (2006), this feedback is amplified by ENSO. The main difference concerns
335 the SST–USTR coupling, which is about 15% greater in the presence of ENSO according to
336 the SFC metric (Table 1; column 1). Interestingly, the amplification of this coupling by ENSO
337 is associated with increased SST variance accounted for by MCA1, while USTR variance

338 remains similar between the two simulations. This means that the equatorial IO SST response
339 to similar variation in wind stress is stronger in the presence than absence of ENSO. Despite
340 similar USTR variance accounted for by SST–USTR MCA1, USTR anomalies are greater
341 along the central equatorial IO in the presence of ENSO (Figs. 2h,i). This suggests that ENSO
342 may modify the IOD-related eastward Sea Level Pressure (SLP) gradient through atmospheric
343 bridge (e.g., Hastenrath 2000) favoring easterly/westerly wind anomalies during boreal fall of
344 developing El Niño/La Niña events (Hastenrath and Polzin 2004), hence boosting the local
345 SST–USTR and SST–20D coupling strength.

346

347 In summary, the model suffers from classical biases found in most state-of-the-art coupled
348 models that lead to imperfect representation of the IOD and a stronger positive Bjerknes
349 feedback during boreal fall (Liu et al. 2014). Second, the IOD-related Bjerknes feedback is
350 amplified by ENSO in our modeling framework, especially the surface wind–SST coupling,
351 which can be attributed to the strong control of ENSO through the Indo-Pacific Walker
352 circulation on the eastward SLP gradient along the equatorial IO during boreal fall.

353

354 **4. Looking for IOD precursors**

355

356 We now seek for identifying the IOD precursors in the observations and the experiments.
357 Figures 3 and 4 show the non-standardized SST EC time series averaged in SON(0) regressed
358 onto standardized anomalies of ocean thermal state (SST and 20D) and atmospheric
359 circulation (850-hPa wind and 200-hPa velocity potential) from SON(0) back to the preceding
360 boreal winter (DJF(0)). The choice of the IOD index (i.e., Saji’s SST or ECs from the
361 different MCA1s) to be regressed does not affect the results. Here, the IOD prediction
362 patterns are expressed in °C for one standard deviation of each local (i.e., at each grid-point)

363 regressor variable to foster direct comparisons between the different seasons, datasets and
364 parameters analyzed.

365

366 4.1 ENSO

367

368 In both observations and CTL, ENSO is one of the main precursors for IOD during late spring
369 and boreal summer since the Pacific SST, the east-west asymmetry of the equatorial Pacific
370 heat content in MAM(0) and JJA(0) (Fig. 3b-c,f-g) and the low-level wind anomalies over the
371 Western North Pacific in MAM(0) (Fig. 4c,g) appear to be good precursors for IOD at these
372 short-time leads. This is consistent with the literature (Annamalai et al. 2003; Li et al. 2003;
373 Gualdi et al. 2003; Bracco et al. 2005; Fischer et al. 2005; Behera et al. 2006). Interestingly,
374 the IOD predictions by the 200-hPa velocity potential fields over the Indo-Pacific region
375 equal to or even outperform the IOD predictions from the tropical Pacific SST at these short
376 time leads. This highlights once again the key-role of ENSO atmospheric teleconnections for
377 boosting the Bjerknes feedback over the IO.

378

379 Significant long-lead (e.g., at 10-12 months time lead) IOD predictions can be traced back to
380 well-known ENSO predictors overcoming the spring predictability barrier in both
381 observations and the CTL (Boschat et al. 2013). In DJF(0), this includes the heat content over
382 the western and central Pacific (Fig. 3d,h) that plays a key-role in the ENSO's recharge
383 oscillator paradigm (Jin et al. 1997; Meinen and McPhaden 2000), and, for CTL only, the
384 low-level zonal wind over the West Pacific (Fig. 4h), whose westerly anomalies may trigger
385 oceanic Kelvin waves propagating into the eastern equatorial Pacific. These results moderate
386 the idea that IOD may help predicting ENSO one year before its peak as an independent
387 precursor (e.g., Izumo et al. 2010; Jourdain et al. 2016) and suggest rather a biennial

388 predictive relationship between IOD and ENSO (Webster and Hoyos 2010). Recently,
389 Stuecker et al. (2015, 2017) argue that IOD predictability is solely determined by ENSO
390 predictability and ENSO signal-to-noise ratio and that the full Tropospheric Biennial
391 Oscillation (TBO; Meehl et al. 2002, 2003) can be fully explained by ENSO dynamics and
392 teleconnections. At first sight, our results are not contradictory with this hypothesis, but the
393 determination of the intrinsic IOD timescale in the FTFC simulation will provide another
394 interpretation in the next section.

395

396 Compared to the observations and the CTL, the IOD prediction patterns simulated over the
397 Pacific in the absence of ENSO (Fig. 4i-l) are poorly significant. This underlines the poor
398 skill of internal noise-related atmospheric variability over the Pacific for IOD prediction.

399

400 4.2 IO tropical-extratropical interactions

401

402 The pIOD prediction patterns of SST (and SLP: not shown) in DJF(0) suggest an active role
403 of the South IO for triggering IOD (Terray and Dominiak 2005; Fischer et al. 2005; Terray et
404 al. 2007; Zhao et al. 2009) with an atmospheric blocking over the extratropical IO that forces
405 a southwest-northeast SST dipole between the southwestern IO, south of Madagascar, and off
406 Australia (Fig. 3d,h). This pattern resembles the SIOD pattern (Behera and Yamagata 2001)
407 and is well captured by the CTL, despite too zonal (Fig. 3h). The mutual predictive
408 relationships between the IOD and SIOD are not discussed thoroughly in the literature to the
409 best of our knowledge and are almost impossible to untangle from observations and fully
410 coupled simulations because both modes are partly forced by ENSO (Schott et al. 2009;
411 Terray 2011). Despite weaker amplitude, this observed SIOD pattern is also well simulated in
412 DJF(0) by FTFC (Fig. 3l), suggesting its validity for IOD triggering even without ENSO. This

413 is further examined in Section 5.4.

414

415 4.3 Tropical IO waves

416

417 A last important long-range precursor for IOD relates to tropical IO oceanic waves (Fig. 3).

418 The IOD prediction pattern derived from 20D anomalies confirms that local oceanic processes

419 are important for IOD (e.g., Webster et al. 1999; Rao et al. 2002; Feng and Meyers 2003).

420 Under ENSO's influence, the observed and simulated IOD prediction patterns from 20D are

421 rather noisy spatially at long time leads (e.g., in DJF(0)), with no evident zonal dipole in the

422 subsurface or significant IOD predictions, especially in the CTL experiment (Fig. 3d,h). This

423 contrasts with the FTFC that displays a strong zonal dipole in DJF(0) (Fig. 3l) that rapidly

424 reverses in sign afterwards, suggesting much biennial IOD variability simulated in the

425 absence of ENSO (Feng and Meyers 2003; Behera et al. 2006), a point at odd with the results

426 of Stuecker et al. (2017) and further discussed in Section 5.

427

428 In summary, the analysis highlights three potential long-range predictors for IOD: ENSO, IO

429 tropical-extratropical interactions that exist without ENSO but are amplified by ENSO, and

430 the role of tropical IO waves, which are damped or even masked in the presence of ENSO.

431 Section 5 seeks for better understanding the influence of these intrinsic IO precursors and

432 timescale without ENSO, as well as their mutual interactions by focusing mostly on the FTFC

433 experiment.

434

435 **5. IOD timescale in the absence of ENSO**

436

437 5.1 IOD timescale

438

439 We first assess the intrinsic timescale (if any) of IOD variability independently of ENSO.
440 This is done by comparing auto and cross-correlations of the various EC time series between
441 the observations and the two experiments (Fig. 5; the corresponding homogenous patterns are
442 displayed in Fig. 2).

443

444 Despite ENSO and IOD are significant precursors of each other at one year lead (see Section
445 4), IOD variability is much more biennial in the absence than presence of ENSO, especially in
446 the subsurface, as demonstrated by the shape of the FTFC auto-correlations of the EC time
447 series (Fig. 5b-c). Interestingly, this biennial rhythm is also seen in the observations (Fig. 5a).
448 The lead-lag correlation analyses between the various EC time series in FTFC (Fig. 5d)
449 confirm this biennial rhythm of the ocean-atmosphere coupling sustained by the subsurface
450 when ENSO is decoupled. These results suggest that the IO is able to sustain a self-contained
451 biennial oscillation, which is at odd with Stuecker et al. (2015, 2017), but consistent with
452 older studies suggesting that IO variability in heat content and ocean dynamics may play a
453 key-role for explaining the reversal in the sign of atmospheric and SST anomalies from one
454 year to another (Feng and Meyers 2003) and sustaining the TBO (Meehl et al. 2002, 2003)
455 independently of ENSO. This IOD–TBO linkage is also consistent with several previous
456 coupled modeling studies, which demonstrate that IOD variability is more biennial when the
457 Pacific is decoupled (Fischer et al. 2005; Behera et al. 2006).

458

459 The biennial rhythm in the FTFC experiment is further assessed by regressing FTFC-climate
460 anomalies in a two-year window onto the 20D standardized SON(0) EC time series derived
461 from the SST–20D MCA1. Main results are few sensitive to the choice of the EC time series
462 considered. Figs. 6 and 7 show regression maps of monthly wind stress, SST and 20D

463 anomalies from Sep(-1) to Nov(0) and from Dec(0) to Nov(+1), respectively. They first
464 confirm the biennial rhythm of the IOD with westerly USTR anomalies along the equator
465 during boreal fall of years (-1) and (+1) coupled to thermocline deepening and SST warming
466 in the eastern equatorial IO (Figs. 6a-c and 7j-l), and reversely during boreal fall of year 0
467 (Fig. 6m-o). The IOD biennial rhythm is, however, much well defined in the eastern IO than
468 in its western part, as reflected by the rather weak and poorly significant SST and subsurface
469 anomalies in the latter during boreal fall of years (-1) and (+1) (Figs. 6a-c and 7j-l).
470 Complementary lead/lag composites highlight also that this biennial rhythm is more sustained
471 by nIOD-to-pIOD than pIOD-to-nIOD transitions (not shown).

472

473 5.2 Role of oceanic waves in the biennial rhythm of IOD

474

475 Figs. 6 and 7 also suggest the importance of both equatorial and off-equatorial oceanic waves
476 for explaining the evolution of the climate anomalies during the two-year window. During
477 boreal fall of year (-1), westerly USTR anomalies along the equator force a fast equatorially-
478 trapped downwelling Kelvin wave that hits Java-Sumatra, deepens the eastern equatorial IO
479 thermocline and warms the central and eastern IO, especially between the equator and 5°S
480 during (Fig. 6b-c). The near-equatorial westerly USTR anomalies relax in early boreal winter
481 and remain weak until mid-spring (Fig. 6d-h). This co-occurs with the reflection of the
482 downwelling Kelvin wave at the eastern boundary into (i) coastal Kelvin waves radiating
483 poleward in both Hemispheres and (ii) near-equatorial downwelling Rossby waves at 3°S and
484 ~3°N (off Java) that both contribute to deepen the thermocline in the eastern tropical IO by
485 Dec(-1) (Fig. 6d). While the downwelling Rossby rapidly weakens at 3°S, it slowly
486 propagates westward until early boreal spring at ~3°N and contributes to damp the negative
487 thermocline anomalies in the Arabian Sea (Fig. 6e-h). Such evolution is reversed from Nov(0)

488 to Apr(+1) (Figs. 6o and 7a-e), consistent with a biennial rhythm.

489

490 Off-equatorial Rossby waves and their westward propagation are also clearly seen in the two-
491 year-window analyzed here (Figs. 6 and 7). Pure pIODs and their associated cold SST
492 anomalies in the eastern IO initiate in Apr-Jun(0) by an anomalous upwelling along the Java-
493 Sumatra coast (Fig. 6i-j). Note that negative 20D anomalies already exist in the eastern
494 equatorial IO during the previous months, providing a favorable preconditioning for pIOD
495 triggering, but are decoupled from the surface before May(0) (Fig. 6f-i). The SST cooling is
496 also coupled with a vigorous anomalous anticyclonic circulation over the southeastern IO
497 during Apr-Jun(0) (Fig. 6h-i). This generates a patch of downwelling pumping over the
498 eastern off-equatorial IO that favors Rossby wave development. The latter slowly propagates
499 westward during the following months, leading to thermocline deepening and SST warming
500 in the western IO (Figs. 6i-o and 7a-c), consistent with previous studies (Rao et al. 2002; Yu
501 et al. 2005; Schott et al. 2009). While these Rossby waves play a pivotal role for shoaling the
502 thermocline in the western tropical IO in boreal fall (Fig. 6m-o), the SST response remains
503 weak there. This relates once again to too deep thermocline simulated on average by the
504 SINTEX model there, even without ENSO. This may explain why the biennial rhythm is less
505 obvious in the SST EC time series (Fig. 5c). This evolution tends finally to be reversed during
506 years (-1) and (+1), but is much less significant (Figs. 6a-c and 7e-l).

507

508 However, the role of these different Rossby waves in reversing the sign of the subsurface
509 anomalies from one year to the next is unclear in the FTFC. Once they have reached the
510 western boundary, the off-equatorial Rossby waves produce persisting 20D anomalies in the
511 western IO during boreal fall and winter (Figs. 6-7) but do not reach the equatorial guide nor
512 propagate eastward along the equator. Thus, they do not seem to help IOD termination during

513 boreal winter, as hypothesized by Feng and Meyers (2003). Similarly, the equatorial Rossby
514 waves do not appear to provide a significant delayed negative feedback to terminate IODs
515 because they dissipate quickly before reaching the western IO boundary and are not reflected
516 as packets of Kelvin waves into the equatorial wave-guide (Figs. 6-7). This also contradicts
517 their suggested key-role in the TBO (Meehl et al. 2003).

518

519 On the other hand, thermocline anomalies between boreal fall and winter appear to be key for
520 IOD transition and explaining changes in the sign of the biennial anomalies. As described
521 above, an equatorially trapped upwelling/downwelling Kelvin wave partly reflects into near-
522 equatorial upwelling/downwelling Rossby waves at the eastern IO boundary during the fall-
523 winter transition succeeding pIOD/nIOD and preceding nIOD/pIOD events, consistent to the
524 oceanic wave reflection theory (Yuan and Liu 2009; Wang and Yuan 2015). This is followed
525 by a sudden inversion in the sign of thermocline anomalies along Java-Sumatra (Fig. 7c-e).
526 The regression of 5-day 20D anomalies along the equator from Sep(-1) to Jun(0) onto
527 monthly 20D anomalies area-averaged in the eastern equatorial IO (sea points within the box
528 shown in Fig. 7b) during Jan(0) (Fig. 8a) confirms the persistence of the eastern equatorial IO
529 20D anomalies after boreal fall and their sudden change in sign during Feb(0). Once the
530 thermocline is reversed in the eastern equatorial IO, the deepening (or shoaling) persists until
531 boreal spring, providing very favorable conditions for nIOD (or pIOD) triggering (Figs. 6-8).
532 The same analysis done using 20D anomalies in Feb(0) as regressor (Fig. 8b) allows focusing
533 on the potential cause of the 20D anomaly reversal during the fall-winter transition. Results
534 demonstrate that these upwelling/downwelling anomalies in Feb(0) are not related to the
535 reflection of the upwelling/downwelling Kelvin wave at the eastern IO boundary. They can be
536 traced back to upwelling/downwelling favorable 20D anomalies in the western IO that
537 propagate eastward and cross the basin in about 20-40 days. This intraseasonal propagating

538 signal is decoupled to monthly USTR anomalies over the eastern equatorial IO during boreal
539 winter, but it may relate to their relaxation over the western and central equatorial IO at this
540 time (Figs. 6e-f and 7b-c) and/or be forced by equatorial westerly wind anomalies at the
541 intraseasonal timescale (Han and Shinoda 2005; Schott et al. 2009).

542

543 5.3 Role of intraseasonal disturbances in the reversal of biennial oceanic and atmospheric 544 anomalies in the IO

545

546 Intraseasonal variability over the equatorial IO from November to February has been
547 suggested as an important factor in the termination of IODs both in observations and
548 simulations (Rao and Yamagata 2004; Han et al. 2006; Rao et al. 2007, 2009). Here, we
549 assess the importance of this factor on the reversal of the biennial IO anomalies when ENSO
550 variability is removed by regressing the fall-to-spring evolution of near-equatorial 5-day
551 outgoing longwave radiation (OLR) and USTR anomalies over the IO onto monthly 20D
552 anomalies area-averaged in the eastern equatorial IO (box in Fig. 7b) during both January and
553 February (Fig. 8c-f). The 20D variability in the eastern equatorial IO is significantly
554 associated with eastward propagating convective disturbances, especially for the February
555 20D anomalies (Fig. 8c-d). These successive intraseasonal convective disturbances are
556 triggered in the western or central IO and reach the eastern IO in about 30 days. This 20–40-
557 day signal is faster than the observed 30–60-day MJO (Han and Shinoda 2005; Schott et al.
558 2009), but is consistent with results obtained with an older version of the SINTEX model
559 (Rao et al. 2007). The associated intraseasonal USTR anomalies may excite equatorial
560 upwelling/downwelling Kelvin waves (Schott et al. 2009) responsible for the
561 shoaling/deepening of the thermocline in the eastern IO in February (Fig. 8b,d,f). This
562 suggests that the MJO is a major contributor to both the termination of IODs and the reversal

563 of the biennial climate anomalies in the absence of ENSO (Han et al. 2006; Rao et al. 2007,
564 2009).

565

566 To further confirm the potential role of the MJO in driven the thermocline reversal occurring
567 between December and February (Figs. 6d-f and 7a-c) in the FTPC, we computed linear
568 correlations at the pentad timescale between 20D anomalies area-averaged in the eastern
569 equatorial IO to zonal anomalies in 20D, OLR and USTR averaged in the 2°S–2°N band. The
570 20D index (box in Fig. 7b) covers a fixed period of 13 pentads centered onto Dec 15, while
571 zonal anomalies cover a sliding period of 13 pentads from 12 pentads prior to 12 pentads after
572 Dec 15. The correlations are performed for each year without any band-pass filtering and are
573 then averaged either over the entire period or for years following pIODs and nIODs. The
574 results (Fig. 9) are very robust since they do not depend on the centering date selected
575 between December 1 and February 1 nor on the choice of the EC time series used to extract
576 IOD events (not shown). They do show propagation of equatorial thermocline anomalies,
577 consistent with Fig. 8b, and a thermocline reversal in the eastern equatorial IO between boreal
578 fall and winter (Fig. 9a-c). This reversal is clearly favored by the MJO, as reflected by
579 positive (negative) correlations with USTR at negative (positive) lags (Fig. 9d-f) and negative
580 correlations with OLR propagating eastward from the western IO to the eastern IO from lag -
581 4 to lag +4. The role of the MJO in the thermocline reversal seems stronger during nIOD-to-
582 pIOD transitions (Fig. 9c,f,i), which exhibit clearer eastward propagating signals than during
583 pIOD-to-nIOD transitions (Fig. 9b,e,h). On the other hand, the IOD variability also modulates
584 the strength of the intraseasonal activity, with nIODs enhancing the MJO in the following
585 boreal winter, consistent with Shinoda and Han (2005).

586

587 5.4 Role of tropical-extratropical IO interactions in IOD triggering

588

589 The subsurface dynamics play a pivotal role for preconditioning IODs and sustaining their
590 biennial rhythm, but are not sufficient for triggering them. This is illustrated in Fig. 10, which
591 shows the monthly evolution of 20D anomalies in the eastern equatorial IO (box in Fig. 7b)
592 before and after pIODs and nIODs in FTPC. This is also consistent with Fig. 6g-j, which
593 shows that pure pIODs/nIODs are triggered by coupled cold/warm SST and
594 anticyclonic/cyclonic circulation anomalies over the southeast IO originating from the
595 extratropical IO.

596

597 The role of such tropical-extratropical IO interactions in triggering pure IODs is further
598 examined with regression maps of quarterly atmospheric and oceanic anomalies from SON(-
599 1) to SON(0) over the tropical-extratropical belt (Figs 11-12). In SON(-1), the abnormally
600 active convection over the eastern equatorial IO associated with nIODs favors local upper-
601 level divergence and shifts westward the Indo-Pacific Walker circulation (Fig. 11a). The
602 upper-level anomalous dipole in velocity potential persists and slowly moves eastward in
603 DJF(0) (Fig. 11a-b), similar to what is observed during ENSO (Lau et Nath, 2000, 2003). The
604 associated convection and diabatic heating anomalies force a Gill-type response immediately
605 westward of them with two low-level cyclonic cells at both sides of the equator and equatorial
606 westerly anomalies. They also excite an atmospheric Rossby wave-train over South IO from
607 SON(-1) to JJA(0) and the associated mid-latitude anomalous SLP pattern slowly propagates
608 eastward in response to the eastward propagation of the diabatic heating anomalies in the
609 tropics (Fig. 11a-d). This suggests that tropical convection over the IO is an important driver
610 for mid-latitude circulation (Cai et al. 2011), with nIOD conditions in SON(-1) strengthening
611 subtropical anticyclones during DJF(0) and associated blocking over the South IO. This
612 atmospheric teleconnection between the tropical and extra-tropical IO in the absence of

613 ENSO generates thus a strong co-variability between boreal fall nIODs and boreal winter
614 positive SIOD events (Fig. 12b,c; Behera and Yamagata 2001), consistent with the fact that
615 SIODs are mainly forced by pulsations of the Mascarene High (Terray 2011; Morioka et al.
616 2012).

617

618 In MAM(0), the SIOD pattern in SST persists and its cold SST anomalies over the southeast
619 IO (Fig. 12c) force a baroclinic circulation over the southeast IO (between Equator and 30°S)
620 with an anomalous 850-hPa anticyclone coupled to anomalous 200-hPa convergence (Fig.
621 11c). These coupled ocean-atmosphere anomalies move northeastward during boreal spring
622 and early summer (Fig. 6g-j), consistent with previous studies (Terray et al. 2007). This
623 significantly affects tropical convection by pushing equatorial convection from the eastern IO
624 to the Maritime Continent and surrounding Western Pacific during MAM(0). These coupled
625 anomalies play also a key-role for triggering IODs after the preconditioning of the subsurface,
626 as discussed in Section 5.2. The low-level anticyclonic anomaly favors easterly wind
627 anomalies along the equator in May(0) (Fig. 6i), which trigger an upwelling Kelvin wave and
628 weaken the Wirtki jet during boreal spring and early summer (Fig. 6i-j). This induces a fast
629 thermocline shoaling over the whole eastern equatorial IO and initiates a positive Bjerknes
630 feedback during Jun(0), promoting the persistence of the eastward equatorial low-level wind
631 and thermocline anomalies there during the following months (Fig. 6i-o). These complex but
632 robust interactions between the tropical and subtropical IO across the seasons are sufficiently
633 strong to impose a well-defined biennial rhythm to IOD variability in the FTPC (Fig. 12).

634

635 **6. Conclusion and discussion**

636

637 This study seeks for examining and understanding the intrinsic IOD precursors and timescale

638 in the absence of ENSO. This is achieved by analyzing a partially decoupled ocean-
639 atmosphere experiment (FTPC) with ENSO variability removed in the tropical Pacific. The
640 FTPC experiment is compared to a fully coupled control (CTL) and observations to
641 disentangle local and remote model biases and the effects of ENSO on IOD, its precursors and
642 timescale.

643

644 First, the IOD does still exist without ENSO as an intrinsic mode of variability, but with
645 reduced amplitude (Figs. 1-2). This is consistent with many previous studies (Fischer et al.
646 2005; Behera et al. 2006; Luo et al. 2010; Santoso et al. 2012; Sun et al. 2015; Wang et al.
647 2016; Cr  tat et al. 2016). Pure IODs have about similar patterns with and without ENSO,
648 indicating IODs take their root within the IO in our modeling framework. Main differences
649 between the two experiments concern a weakened Bjerknes feedback in the absence of
650 ENSO, especially the SST–USTR coupling that is about 15% weaker (Fig. 2 and Table 1).
651 Our results show that ENSO amplifies the IOD-related Bjerknes feedback by modifying the
652 eastward SLP gradient and the associated zonal wind anomalies over the equatorial IO
653 through the atmospheric bridge (e.g., Hastenrath 2000; Hastenrath and Polzin 2004). More
654 importantly, the IOD timescale greatly differs between the two experiments (Fig. 5). IOD
655 timescale appears to be much more biennial in the absence of ENSO, in line with Feng and
656 Meyers (2003) and Behera et al. (2006). This IOD biennial rhythm is much clearer in the
657 subsurface than at the surface and in the eastern than the western IO (Figs. 6-7). This biennial
658 rhythm is also found for the recent observations, consistent with Meehl et al. (2002, 2003) and
659 Webster and Hoyos (2010), but surprisingly not in our 200-yr long CTL. This differs from
660 Stuecker et al. (2017) who argue that IOD biennial timescale can be fully explained by
661 ENSO. The reasons of this difference are not due to improper simulated ENSO periodicity
662 that is fairly well captured by the CTL (Masson et al. 2012; Terray et al. 2016). The

663 hypothesis that the IOD timescale and TBO may be solely explained by ENSO dynamics
664 (Stuecker et al. 2015, 2017) is thus not consistent with our modeling results since the
665 experiment with ENSO does not simulate biennial IOD timescale, while the experiment
666 without ENSO does.

667

668 Despite IOD has its own timescale, ENSO appears as one of the main short- and long-time
669 lead precursors for IOD in the observations and the CTL, confirming the CTL accurately
670 simulates ENSO influence on IOD. Apart from ENSO, two long-time IOD precursors are
671 found within the IO. The first involves tropical-extratropical interactions linking the IOD and
672 the SIOD (Behera and Yamagata 2001) that exist without ENSO but are amplified by ENSO.
673 The second involves the subsurface and Kelvin waves in the equatorial IO. This oceanic
674 precursor, which is intimately associated with the IOD biennial timescale, is damped or even
675 masked in the presence of ENSO because of the influence of the associated Walker
676 circulation anomalies on the equatorial IO zonal wind (Hastenrath and Polzin 2004). A
677 detailed analysis points toward a complementary role between equatorial subsurface dynamics
678 and tropical-extratropical interactions in preconditioning and triggering IOD events,
679 respectively, and in sustaining the biennial oscillation over the IO when ENSO is decoupled.
680 In our modeling framework, reflections of equatorial and off-equatorial oceanic waves on the
681 western and eastern IO boundaries cannot explain the IOD biennial timescale, contrary to
682 previous hypotheses (Feng and Meyers 2003; Meehl et al. 2002, 2003).

683

684 Our results suggest that the rapid reversal of the thermocline anomalies during the decaying
685 phase of pure IODs (i.e., during December–February in the FTFC experiment) is key for
686 preconditioning subsequent IOD development of opposite sign the next year. This sudden
687 reversal relates to intraseasonal disturbances reminiscent of the MJO during boreal winter

688 following IOD events, especially after negative IOD events. This complements the influence
689 of the MJO on IOD termination reported in both observations and simulations (Rao and
690 Yamagata 2004; Han et al. 2006; Rao et al. 2007, 2009) by showing that MJO and IOD are
691 tightly interconnected. Such coupling between the MJO and the IO subsurface is, however,
692 not sufficient for triggering pure IODs (Fig. 10).

693

694 Such triggering originates from the extratropical IO (Figs. 6-7 and 11-12), consistent with
695 several previous studies (Terray and Dominiak 2005; Fischer et al. 2005; Terray et al. 2007;
696 Zhao et al. 2009). Here, we show complex two-way interactions between IOD and SIOD.
697 First, IOD-related convection forces the mid-latitude circulation (Cai et al. 2011; Morioka et
698 al. 2012), with nIOD conditions strengthening the South IO anticyclone and associated
699 blocking during boreal winter, hence promoting positive SIOD events. Second, this blocking
700 and associated cold SST anomalies over the southeast IO persist until the subsequent boreal
701 spring and force an anomalous anticyclonic circulation at the surface over the southeast IO.
702 Such coupled ocean-atmosphere anomalies over the southeast IO are fundamental for
703 triggering IODs during boreal spring after the preconditioning of the subsurface in boreal
704 winter. The reverse prevails for pIOD conditions.

705

706 These complementary influences of equatorial IO dynamics, intraseasonal atmospheric
707 disturbances and tropical-extratropical interactions in triggering IOD and promoting biennial
708 variability may shed new lights for improving our ability to predict IOD and its climate
709 impacts.

710

711 **Acknowledgments**

712

713 This work was funded by the Earth System Science Organization, Ministry of Earth Sciences,
714 Government of India under Monsoon Mission (Project No. MM/SERP/CNRS/2013/INT-
715 10/002 Contribution #MM/PASCAL/RP/07. This work was performed using HPC resources
716 from GENCI-IDRIS (Grants 2015, 2016, 2017 – 016895).
717

718 **References**

719

720 Annamalai H, R Murtugudde, J Potemra, SP Xie, P Liu, B Wang (2003) Coupled dynamics
721 over the Indian Ocean: Spring initiation of the zonal mode. *Deep-Sea Res II*, 50:2305–
722 2330

723 Ashok K, Z Guan, T Yamagata (2003) A look at the relationship between the ENSO and the
724 Indian Ocean dipole. *J Meteor Soc Japan*, 81:41–56

725 Battisti DS, AC Hirst (1989) Interannual variability in the tropical atmosphere-ocean system:
726 influences of the basic state, ocean geometry and nonlinearity. *J Atmos Sci* 46:1687–
727 1712

728 Behera SK, T Yamagata (2001) Subtropical SST dipole events in the southern Indian Ocean.
729 *Geophys Res Lett* 28:327–330

730 Behera SK, JJ Luo, S Masson, P Delecluse, S Gualdi, A Navarra, T Yamagata (2005)
731 Paramount impact of the Indian Ocean dipole on the East African short rains: A CGCM
732 study. *J Clim* 18:4514–4530

733 Behera SK, JJ Luo, S Masson, SA Rao, H Sakuma, T Yamagata (2006) A CGCM study on
734 the interaction between IOD and ENSO. *J Clim* 19:1608–1705

735 Black E, J Slingo, KR Sperber (2003) An observational study of the relationship between
736 excessively strong short rains in coastal East Africa and Indian Ocean SST. *Mon Wea*
737 *Rev* 131:74–94

738 Boschat G, P Terray, S Masson (2013) Extratropical forcing of ENSO. *Geophys Res Lett*
739 40:1–7

740 Bracco A, F Kucharski, F Molteni (2005) Internal and forced modes of variability in the
741 Indian Ocean. *Geophys Res Lett* 32, L12707, doi:10.1029/2005GL023154

742 Bretherton CS, C Smith, JM Wallace (1992) An intercomparison of methods for finding
743 coupled patterns in climate data. *J Clim* 5:541–560

744 Cai W, A Sullivan, T Cowan T (2009) Climate change contributes to more frequent
745 consecutive positive Indian Ocean dipole events. *Geophys Res Lett* 36, L23704,
746 doi:10.1029/2009GL040163

747 Cai W, P van Rensch, T Cowan, HH Hendon (2011) Teleconnection pathways of ENSO and
748 the IOD and the mechanisms for impacts on Australian rainfall. *J. Climate*, 24 :3910–
749 3923

750 Cai W, T Cowan (2013) Why is the amplitude of the Indian Ocean Dipole overly large in
751 CMIP3 and CMIP5 climate models?. *Geophys Res Lett* 40:1200-1205,
752 doi:10.1002/grl.50208

753 Chan SC, SK Behera, T Yamagata (2008) Indian Ocean Dipole influence on South American
754 rainfall. *Geophys Res Lett* 35:L14S12, doi:10.1029/2008GL034204

755 Compo GP, P Sardeshmukh (2010) Removing ENSO-related variations from the climate
756 records. *J Clim* 23:1957–1978

757 Compo GP and Coauthors (2011) The twentieth century reanalysis project. *Q J R Meteorol*
758 *Soc* 137:1–28

759 Crétat J, P Terray, S Masson, KP Sooraj, MK Roxy (2016) Indian Ocean and Indian summer
760 monsoon: relationships without ENSO in ocean-atmosphere coupled simulations. *Clim*
761 *Dyn*, online, doi:10.1007/s00382-016-3387-x

762 Dee DP and Coauthors (2011) The ERA-Interim reanalysis: configuration and performance of
763 the data assimilation system. *Q J R Meteorol Soc* 137:553–597

764 Delman AS, J Sprintall, JL McClean, LD Talley (2016) Anomalous Java cooling at the
765 initiation of positive Indian Ocean Dipole events. *J Geophys Res Oc*,
766 doi:10.1002/2016JC011635

767 Doi T, SK Behera, T Yamagata (2016) Improved seasonal prediction using the SINTEX-F2
768 coupled model. *J Adv Mod Earth Syst* 8:1847–1867

769 Drbohlav HKL, S Gualdi, A Navarra (2007) A diagnostic study of the Indian Ocean dipole
770 mode in El Niño and non-El Niño years. *J Clim* 20:2961–2977

771 Feng M, G Meyers (2003) Interannual variability in the tropical Indian Ocean: a two-year
772 time-scale of Indian Ocean Dipole. *Deep-Sea Res II* 50:2263–2284

773 Fischer AS, P Terray, P Delecluse, S Gualdi, E Guilyardi (2005) Two independent triggers for
774 the Indian Ocean dipole/zonal mode in a coupled GCM. *J Clim* 18:3428–3449

775 Gadgil S, PN Vinayachandran, PA Francis, S Gadgil (2004) Extremes of the Indian summer
776 monsoon rainfall, ENSO and equatorial Indian Ocean oscillation. *Geophys Res Lett* 31,
777 L12213, doi:10.1029/2004GL019733

778 Giese BS, S Ray (2011) El Niño variability in simple ocean data assimilation (SODA), 1871–
779 2008. *J Geophys Res* 116:C02024, doi:10.1029/2010JC006695

780 Gualdi S, E Guilyardi, A Navarra, S Masina, P Delecluse (2003) The interannual variability in
781 the tropical Indian Ocean as simulated by a CGCM. *Clim Dyn* 20:567–582

782 Guo F, Q Liu, XT Zheng, S Sun (2013) The role of barrier layer in Southeastern Arabian Sea
783 during the development of positive Indian Ocean Dipole events. *Ocean Coast Res*
784 12:245–252

785 Guo F, Q Liu, S Sun, J Yang (2015) Three types of Indian Ocean Dipoles. *J Clim* 28:3073–
786 3092

787 Han W, T Shinoda, LL Fu, JP McCreary (2006) Impact of atmospheric intraseasonal
788 oscillations on the Indian Ocean dipole during the 1990s. *J Phys Oceanogr* 111:679–690

789 Hastenrath S (2000) Zonal circulations over the equatorial Indian Ocean. *J Clim* 13:2746–
790 2756

791 Hastenrath S, D Polzin (2004) Dynamics of the surface wind field over the equatorial Indian
792 Ocean. *Q J R Meteorol Soc* 130:503-517

793 Hendon HH (2003) Indonesian rainfall variability: impact of ENSO and local air–sea
794 interaction. *J Clim* 16:1775–1790

795 Hong CC, T Li, YC LinHo Chen (2010) Asymmetry of the Indian Ocean basinwide SST
796 anomalies: roles of ENSO and IOD. *J Clim* 23:3563–3576

797 Izumo T, J Vialard, M Lengaigne, C de Boyer Montégut, SK Behera, JJ Luo, S Cravatte, S
798 Masson, T Yamagata (2010) Influence of the state of the Indian Ocean Dipole on the
799 following year’s El Niño. *Nature Geoscience* 3:168–172

800 Jin FF (1997) An equatorial ocean recharge paradigm for ENSO. Part I: conceptual model. *J*
801 *Atmos Sci* 54:811–829

802 Jourdain NC, M Lengaigne, J Vialard, T Izumo, AS Gupta (2016) Further insights on the
803 influence of the Indian Ocean Dipole on the following year’s ENSO from observations
804 and CMIP5 models. *J Clim* 29:637–658

805 Kajikawa Y, T Yasunari, R Kawamura (2003) The role of the local Hadley circulation over
806 the Western Pacific on the zonally asymmetric anomalies over the Indian Ocean. *J*
807 *Meteor Soc Japan* 81:259–276

808 Kajtar JB, A Santoso, MH England, W Cai (2016) Tropical climate variability: interactions
809 across the Pacific, Indian, and Atlantic Oceans. *Clim Dyn*, doi:10.1007/s00382-016-
810 3199-z

811 Klein SA, BJ Soden, NC Lau (1999) Remote sea surface temperature variations during
812 ENSO: evidence for a tropical atmospheric bridge. *J Clim* 12:917–932

813 Krishnaswamy J, S Vaidyanathan, B Rajagopalan, M Bonell, M Sankaran, RS Bhalla, S
814 Badiger (2015) Non-stationary and non-linear influence of ENSO and Indian Ocean

815 Dipole on the variability of Indian monsoon rainfall and extreme rain events. *Clim Dyn*
816 45:175–184

817 Lau NC, MJ Nath (2000) Impact of ENSO on the variability of the Asian–Australian
818 monsoons as simulated in GCM experiments. *J Clim* 13:4287–4309

819 Lau NC, MJ Nath (2003) Atmosphere–ocean variations in the Indo-Pacific sector during
820 ENSO episode. *J Clim* 16:3–20

821 Li T, B Wang, CP Chang, YS Zhang (2003) A theory for the Indian Ocean dipole-zonal
822 mode. *J Atmos Sci* 60:2119–2135

823 Liu L, SP Xie, XT Zheng, T Li, Y Du, G Huang, WD Yu (2014) Indian Ocean variability in
824 the CMIP5 multi-model ensemble: the zonal dipole mode. *Clim Dyn* 43:1715–1730

825 Liu H, Y Tang, D Chen, T Lian (2016) Predictability of the Indian Ocean Dipole in the
826 coupled models. *Clim Dyn*, doi:10.1007/s00382-016-3187-3

827 Luo JJ, S Masson, S Behera, S Shingu, T Yamagata (2005) Seasonal climate predictability in
828 a coupled OAGCM using a different approach for ensemble forecasts. *J Clim* 18 :4474–
829 4497

830 Luo JJ, R Zhang, S Behera, Y Masumoto, FF Jin, R Lukas, T Yamagata (2010) Interactions
831 between El Nino and extreme Indian Ocean dipole. *J Clim* 23: 726-742

832 Madec G (2008) NEMO ocean engine. Note du Pôle de modélisation, Institut Pierre-Simon
833 Laplace (IPSL), France. No 27. ISSN No 1288-1619

834 Masson S, P Terray, G Madec, JJ Luo, T Yamagata, K Takahashi (2012) Impact of intra-daily
835 SST variability on ENSO characteristics in a coupled model. *Clim Dyn* 39:681–707

836 McPhaden MJ (1999) Genesis and evolution of the 1997–1998 El Niño. *Science* 283:950–954

837 McPhaden MJ, M Nagura (2014) Indian Ocean dipole interpreted in terms of recharge
838 oscillator theory. *Clim Dyn* 42:1569–1586

839 Meehl GA, JM Arblaster (2002) Indian monsoon GCM sensitivity experiments testing
840 tropospheric biennial oscillation transition conditions. *J Clim* 15:923–944

841 Meehl GA, JM Arblaster, J Loschnigg (2003) Coupled ocean–atmosphere dynamical
842 processes in the tropical Indian and Pacific Oceans and the TBO. *J Clim* 16:2138–2158

843 Meinen CS, MJ McPhaden (2000) Observations of warm water volume changes in the
844 equatorial Pacific and their relationship to El Niño and La Niña. *J Clim* 13:3551–3559

845 Morioka Y, S Masson, P Terray, JJ Luo, T Yamagata (2012) Subtropical dipole modes
846 simulated in a coupled general circulation model. *J Clim* 25:4029–4047

847 Murtugudde R, JP McCreary Jr, AJ Busalacchi (2000) Oceanic processes associated with
848 anomalous events in the Indian Ocean with relevance to 1997–1998. *J Geophys Res*
849 105:3295–3306

850 Prodhomme C, P Terray, S Masson, T Izumo, T Tozuka, T Yamagata (2014) Impacts of
851 Indian Ocean SST biases on the Indian monsoon: as simulated in a global coupled
852 model. *Clim Dyn* 42:271–290

853 Prodhomme C, P Terray, S Masson, G Boschhat, T Izumo (2015) Oceanic factors controlling
854 the Indian summer monsoon onset in a coupled model. *Clim Dyn* 44:977–1002

855 Rao SA, SK Behera, Y Masumoto, T Yamagata (2002) Interannual subsurface variability in
856 the Tropical Indian Ocean with a special emphasis on the Indian Ocean Dipole. *Deep-*
857 *Sea Res* 49:1549–1572

858 Rao SA, T Yamagata (2004) Abrupt termination of Indian Ocean dipole events in response to
859 intraseasonal disturbances, *Geophys Res Lett* 31, L19306, doi:10.1029/2004GL020842

860 Rao SA, SK Behera (2005) Subsurface influence on SST in the tropical Indian Ocean:
861 structure and interannual variability. *Dyn Atmo Oceans* 39:103–135

862 Rao SA, S Masson, JJ Luo, SK Behera, T Yamagata (2007) Termination of Indian Ocean
863 Dipole events in a coupled general circulation model. *J Clim* 20:3018–3035

864 Rao SA, JJ Luo, SK Behera, T Yamagata (2009) Generation and termination of Indian Ocean
865 dipole events in 2003, 2006 and 2007. *Clim Dyn* 33:751–767

866 Rayner NA, DE Parker, EB Horton, CK Folland, LV Alexander, DP Rowell, EC Kent, A
867 Kaplan (2003) Global analyses of sea surface temperature, sea ice, and night marine air
868 temperature since the late nineteenth century *J Geophys Res* 108,
869 doi:10.1029/2002JD002670

870 Roeckner E, G Baüml, L Bonaventura, R Brokopf, M Esch, M Giorgetta, S Hagemann et al
871 (2003) The atmospheric general circulation model ECHAM5: Part 1: model description.
872 Max-Planck-Institut für Meteorologie, MPI-Report 353, Hamburg

873 Saji NH, BN Goswami, PN Vinayachandran, T Yamagata (1999) A dipole mode in the
874 tropical Indian Ocean. *Nature* 401:360–363

875 Saji NH, T Yamagata (2003) Possible impacts of Indian Ocean Dipole mode events on global
876 climate. *Clim Res* 25:151–169

877 Santoso A, MH England, W Cai (2012) Impact of Indo-Pacific feedback interactions on
878 ENSO dynamics diagnosed using ensemble climate simulations. *J Clim* 25:7743–7763

879 Schott FA, SP Xie, JP McCreary Jr (2009) Indian Ocean circulation and climate variability
880 *Rev Geophys* 47, RG1002, doi:10.1029/2007RG000245

881 Shi L, HH Hendon, O Alves, JJ Luo, M Balmaseda, D Anderson (2012) How predictable is
882 the Indian Ocean Dipole? *Mon Weather Rev* 140:3867–3884

883 Shinoda T, HH Hendon, MA Alexander (2004a) Surface and subsurface dipole variability in
884 the Indian Ocean and its relation to ENSO. *Deep Sea Res* 51:619–635

885 Shinoda T, MA Alexander, HH Hendon (2004b) Remote response of the Indian Ocean to
886 interannual SST variations in the tropical Pacific. *J Clim* 17:362–372

887 Shinoda T, W Han (2005) Influence of the Indian Ocean Dipole on atmospheric subseasonal
888 variability. *J Clim* 18:3891–3909

889 Spencer H, RT Sutton, JM Slingo, JM Roberts, E Black (2005) The Indian Ocean climate and
890 dipole variability in the Hadley centre coupled GCMs. *J Clim* 18:2286–2307

891 Sprintall J, A Révelard (2014) The Indonesian throughflow response to Indo-Pacific climate
892 variability. *J Geophys Res Oceans* 119, 1161–1175, doi:10.1002/2013JC009533

893 Stuecker MF, A Timmermann, J Yoon, F-F Jin (2015) Tropospheric biennial oscillation
894 (TBO) indistinguishable from white noise, *Geophys Res Lett* 42:7785–7791

895 Stuecker MF, A Timmermann, F-F Jin, Y Chikamoto, W Zhang, AT Wittenberg, E Widiasih,
896 and S. Zhao (2017) Revisiting ENSO/Indian Ocean Dipole phase relationships,
897 *Geophys Res Lett* 44:2481–2492

898 Sun S, J Lan, Y Fang, Tana, X Gao (2015) A triggering mechanism for the Indian Ocean
899 dipoles independent of ENSO. *J Clim* 28:5063–5076

900 Suzuki R, SK Behera, S Iizuka, T Yamagata (2004) Indian Ocean subtropical dipole
901 simulated using a coupled general circulation model. *J Geophys Res* 109,
902 doi:10.1029/2003JC001974

903 Terray P, S Dominiak (2005) Indian Ocean sea surface temperature and El Niño and Southern
904 Oscillation: a new perspective. *J Clim* 18:1351–1368

905 Terray P, S Dominiak, P Delecluse (2005) Role of the southern Indian Ocean in the
906 transitions of the monsoon-ENSO system during recent decades. *Clim Dyn* 24:169–195

907 Terray P, F Chauvin, H Douville (2007) Impact of southeast Indian Ocean sea surface
908 temperature anomalies on monsoon-ENSO dipole variability in a coupled ocean-
909 atmosphere model. *Clim Dyn* 28:553–580

910 Terray P, K Kamala, S Masson, G Madec, AK Sahai, JJ Luo, T Yamagata (2012) The role of
911 the intra-daily SST variability in the Indian monsoon variability and monsoon-ENSO–
912 IOD relationships in a global coupled model. *Clim Dyn* 39:729–754

913 Terray P, S Masson, C Prodhomme, MK Roxy, KP Sooraj (2016) Impacts of Indian and

914 Atlantic oceans on ENSO in a comprehensive modeling framework. *Clim Dyn*
915 46:2507–2533

916 Timmermann R, H Goosse, G Madec, T Fichefet, C Etche, V Duliere (2005) On the
917 representation of high latitude processes in the ORCA-LIM global coupled sea ice-
918 ocean model. *Ocean Model* 8(1–2):175–201

919 Tozuka T, JJ Luo, S Masson, T Yamagata (2007) Decadal modulations of the Indian Ocean
920 dipole in the SINTEX-F1 coupled GCM. *J Clim* 20:2881–2894

921 Ummenhofer CC, MH England, GA Meyers, PC McIntosh, MJ Pook, JS Risbey, A Sen
922 Gupta, and AS Taschetto (2009) What causes southeast Australia’s worst droughts?
923 *Geophys Res Lett*, 36:L04706, doi:10.1029/2008GL036801

924 Valcke S (2006) OASIS3 user guide (prism_2-5). PRISM support initiative report No 3, 64 pp

925 Vecchi GA, DE Harrison (2000) Tropical Pacific sea surface temperature anomalies, El Niño
926 and equatorial westerly events. *J Clim* 13:1814–1830

927 Wallace JM, C Smith, Q Jiang Q (1990) Spatial patterns of ocean–atmosphere interaction in
928 the northern winter. *J Clim* 3:990–998

929 Wang X, C Wang (2014) Different impacts of various El Niño events on the Indian Ocean
930 Dipole. *Clim Dyn* 42:991–1005

931 Wang J, D Yuan (2015) Roles of western and eastern boundary reflections in the interannual
932 sea level variations during negative Indian Ocean Dipole events. *J Phys Ocean*
933 45:1804–1821

934 Wang H, R Murtugudde, A Kumar (2016) Evolution of Indian Ocean dipole and its forcing
935 mechanisms in the absence of ENSO. *Clim Dyn*, doi:10.1007/s00382-016-2977-y

936 Webster PJ, Moore AM, Loschnigg JP, Leben RR (1999) Coupled ocean–atmosphere
937 dynamics in the Indian Ocean during 1997–98. *Nature* 401:356–360

938 Webster PJ, Hoyos CD (2010) Beyond the spring barrier? *Nature Geoscience* 3:152–153

- 939 Wyrski K (1985) Water displacements in the Pacific and the genesis of El Niño cycles. *J*
940 *Geophys Res Oceans* 90:7129–7132
- 941 Xie S-P, H Annamalai, F Schott, JP McCreary Jr. (2002) Origin and predictability of South
942 Indian Ocean climate variability, *J Clim.*, 15:864–874
- 943 Yamagata T, SK Behera, JJ Luo, S Masson , MR Jury, SA Rao (2004) Coupled ocean-
944 atmosphere variability in the tropical Indian Ocean. *Geophysical Monograph Series*
945 (eds) Wang C, Xie S P and Carton JA 147, 414 pp
- 946 Yang Y, SP Xie, L Wu, Y Kosoka, NC Lau, GA Vecchi (2015) Seasonality and predictability
947 of the Indian Ocean Dipole mode: ENSO forcing and internal variability. *J Clim*
948 28:8021–8036
- 949 Yuan D, H Liu (2009) Long wave dynamics of sea level variations during Indian Ocean
950 dipole events. *J Phys Oceanogr* 39:1115–1132
- 951 Yuan DL and Coauthors (2011) Forcing of the Indian Ocean Dipole on the interannual
952 variations of the tropical Pacific Ocean: Roles of the Indonesian Throughflow. *J Clim*
953 24:3593–3608
- 954 Yu J, KM Lau (2004) Contrasting Indian Ocean SST variability with and without ENSO
955 influence: a coupled atmosphere-ocean GCM study. *Meteor Atmos Phys* 90, doi:
956 10.1007 /s00703-004-0094-7
- 957 Yu W, B Xiang, L Liu, N Liu (2005) Understanding the origins of interannual thermocline
958 variations in the tropical Indian Ocean. *Geophys Res Lett* 32:L24706,
959 doi:10.1029/2005GL024327
- 960 Zhang Q, J Gottschalk (2002) SST anomalies of ENSO and the Madden–Julian oscillation in
961 the equatorial Pacific. *J Clim* 15:2429–2445
- 962 Zhang Y, JR Norris, JM Wallace (1998) Seasonality of large scale atmosphere–ocean
963 interaction over the North Pacific. *J Clim* 11:2473–2481

- 964 Zhao M, HH Hendon (2009) Representation and prediction of the Indian Ocean dipole in the
965 POAMA seasonal forecast model. *Quart J Roy Meteor Soc* 135:337–352
- 966 Zhao YP, YL Chen, F Wang, XZ Bai, AM Wu (2009) Two modes of dipole events in tropical
967 Indian Ocean. *Sci China Ser D-Earth Sci* 52:369–381
- 968

969 **Figure Captions**

970

971 **Figure 1:** (a) September–November SST (shadings every 0.05 K) and 20°C isotherm
972 depth (20D; contours every 1 m; green/purple contours for shallow/deep thermocline)
973 anomalies regressed onto the normalized boreal fall (i.e., SON) IOD index from Saji et al.
974 (1999) for the 1979-2008 observations. (b) Same as (a) but for rainfall (shadings every 0.25
975 mm.day⁻¹) and 850-hPa wind (vectors; m.s⁻¹) anomalies. (c-d) and (e-f) Same as (a-b) but for
976 the CTL and the FTPC experiments, respectively. Anomalies that are not significant at the
977 90% confidence level according to a bootstrap test are masked. See Section 2.3 for details on
978 the bootstrap test.

979

980 **Figure 2:** (a) SST homogeneous map of the first leading MCA mode (MCA1) between
981 monthly SST and 20D anomalies during boreal fall (September to November) for the 1979-
982 2008 observations. (b-c) Same as (a) but for the CTL and FTPC experiments, respectively. (d-
983 f) and (g-i) Same as (a-c) but for the 20D mode derived from the SST–20D MCA1 and for the
984 USTR mode derived from the SST–USTR MCA1, respectively. Units are labeled on the
985 Figure. Summary statistics for the different MCA1s are given in Tables 1-3.

986

987 **Figure 3:** (a-d) IOD prediction patterns of SST (shadings every 0.5 K) and 20D (contours
988 every 1 K; green/purple contours for negative/positive coefficients and black contours for
989 nullity) from the IOD peak season at year 0 (SON(0)) back to the preceding boreal winter
990 (DJF(0)) for the observations. (e-h) and (i-l) Same as (a-d) but for the CTL and the FTPC,
991 respectively. The IOD prediction patterns are obtained by regressing the non-normalized 20D
992 EC time series derived from SST–20D MCA1 and averaged in SON(0) onto normalized
993 quarterly anomalies at the grid point scale from SON(0) back to DJF(0). Significance tested at

994 the 90% confidence level as in Fig. 1. Only significant IOD predictions are shown for 20D.
995 Significant IOD predictions are shown with black dots for SST.

996

997 **Figure 4:** Same as Fig. 3 but for the IOD prediction patterns derived from 200-hPa
998 velocity potential (shadings every 0.5 K) and 850-hPa zonal wind (contours every 1 K;
999 dotted/solid contours for negative/positive coefficients) anomalies. Only significant IOD
1000 predictions at the 90% confidence level are shown for 850-hPa zonal winds. IOD predictions
1001 significant at the 90% confidence level are shown with black dots for 200-hPa velocity
1002 potential.

1003

1004 **Figure 5:** (a) Autocorrelation in the monthly SST, 20D and USTR EC time series. (b-c)
1005 Same as (a) but for the CTL and the FTFC, respectively. (d) Cross-correlation between the
1006 three EC time series for the FTFC. The EC time series are computed by projecting the
1007 monthly anomalies over the equatorial IO (10°S–10°N) for each variable onto the
1008 corresponding singular vectors derived from SST–20D MCA1 for SST and 20D and from
1009 SST–USTR MCA1 for USTR.

1010

1011 **Figure 6:** Monthly SST (contours every 0.05 K; blue/red contours for SST
1012 cooling/warming and black contours for nullity), 20D (shadings every 1 K; cool/warm
1013 shadings for thermocline shoaling/deepening) and wind stress (vectors; Pascal) anomalies
1014 from (a) Sep(-1) to (o) Nov(0) regressed onto the normalized 20D EC time series from SST–
1015 20D MCA1 averaged during SON(0) for the FTFC experiment. Significance tested at the 90%
1016 confidence level as in Fig. 1. Only significant regression coefficients are shown for SST and
1017 20D. Significant regression coefficients are shown by thick black arrows for wind stress.

1018

1019 **Figure 7:** Same as Fig. 6 but from (a) Dec(0) to (l) Nov(+1). The black box in panel b
1020 shows the domain used for computing the 20D index in Section 5.

1021

1022 **Figure 8:** (a) Regression of 5-day 20D anomalies area-averaged in the 2°S – 2°N band
1023 from September to June onto monthly 20D anomalies in the eastern equatorial IO (box shown
1024 in Fig. 7b) during January in the FTPC experiment. (b) Same as (a) but with the monthly 20D
1025 index in February. (c-d) and (e-f) Same as (a-b) but for 5-day OLR and USTR anomalies,
1026 respectively. Positive/Negative OLR and USTR anomalies correspond to
1027 weakened/strengthened convection and westerly/easterly wind anomalies, respectively. Black
1028 contours show significant regression coefficients at the 90% confidence level tested as in Fig.
1029 1.

1030

1031 **Figure 9:** Lead/lag pentad correlations between 20D anomalies area-averaged in the
1032 eastern equatorial IO (box in Fig. 7b) and zonal IO anomalies in (a-c) 20D, (d-f) USTR and
1033 (g-i) OLR averaged in the band 2°S – 2°N for the FTPC experiment. Time series of both 20D
1034 index and climate zonal anomalies span 13 pentads. The 20D index is fixed and centered onto
1035 Dec 15, while climate zonal anomalies slide from 12 pentads ahead to 12 pentads after Dec
1036 15, every 1 pentad. Lag 0 corresponds to the synchronous correlation (i.e., centered onto Dec
1037 15). The direction of the lead/lag relationship is labeled on each panel. First, second and third
1038 columns correspond to lead/lag correlations averaged over the entire simulation period and for
1039 years following the 10% most intense pIODs and nIODs, respectively. The 10% most intense
1040 p/nIODs events are defined when the 20D EC time series (derived from SST–20D MCA1)
1041 averaged during SON is below/above its 10th/90th percentile threshold value. Significance is
1042 computed for each year at the 90% confidence level according to the Bravais-Pearson test.

1043 Light-to-dark contours show significant correlations reached 50% to 90% of the years, every
1044 10%.

1045

1046 **Figure 10:** (a-b) Monthly evolution of 20D anomalies (m), area-averaged in the eastern
1047 equatorial IO (box in Fig. 7b), one year back to the occurrence of pIODs and nIODs,
1048 respectively. (c-d) Same as (a-b) but one year after p/nIODs. Thin curves represent the 20D
1049 evolution of the 10% most intense IOD events (see Fig. 9 for definition) and thick curve is the
1050 ensemble mean.

1051

1052 **Figure 11:** Regression of quarterly SLP (contours every 10 Pa, blue/red contour for
1053 low/high pressure and black contour for nullity), 200-hPa velocity potential (shadings every 1
1054 $\times 10^4 \text{ m}^2 \cdot \text{s}^{-1}$; cold/warm colors for upper-level divergence/convergence) and 850-hPa wind
1055 (vectors; $\text{m} \cdot \text{s}^{-1}$) anomalies regressed from (a) SON(-1) to (e) SON(0) onto the normalized 20D
1056 EC time series (derived from the SST–20D MCA1) in SON(0) for the FTPC experiment.
1057 Regression coefficients that are not significant at the 90% confidence level according to a
1058 bootstrap test are masked for SLP and 200-hPa velocity potential. Significant regression
1059 coefficients are shown by thick black arrows for 850-hPa wind.

1060

1061 **Figure 12:** Same as Fig. 11 but for the regressions of 20D (shadings) and SST (contours)
1062 anomalies. Regression coefficients that are not significant at the 90% confidence level
1063 according to a bootstrap test are masked for SST. Significant 20D anomalies at the 90%
1064 confidence level are shown with black dots.

1065

1066 **Table Captions**

1067

1068 **Table 1:** Summary statistics for the first SST–USTR MCA leading mode (MCA1)
1069 applied onto 10°S–10°N monthly anomalies during boreal fall (September to November) in
1070 the observations and the two experiments.

1071

1072 **Table 2:** Same as Table 1 but for the SST–20D MCA1.

1073

1074 **Table 3:** Same as Table 1 but for the 20D–USTR MCA1.

1075

1076 **Tables**

1077

1078

	SFC (%)	NC (%)	r inter-EC: SST – USTR	SSTvar (%)	USTRvar (%)	r EC – IOD Saji		r EC – IOD SINTEX	
						SST	USTR	SST	USTR
OBS	92.7	29.53	0.68	44.48	41.78	0.88	0.85	/	/
CTL	91.78	26.11	0.74	39.82	31.46	0.86	0.78	0.90	0.83
FTPC	79.13	22.25	0.69	33.99	30.77	0.78	0.65	0.84	0.71

1079

1080

1081

1082

1083

1084

1085

1086

1087

1088

The SCF gives the fraction of the square covariance between SST and USTR explained by MCA1. The NC and inter-EC correlation (r) assess the strength of the SST–USTR coupling. SSTvar and USTRvar are the variance of SST and USTR explained by their respective expansion coefficient (EC) time series. The correlation r between each EC time series and the IOD as defined by Saji et al. (1999), both averaged during SON, quantifies how well MCA1 summarizes the IOD variability. Similar r correlation is computed for the two experiments but with the 5°S–5°N band removed from the western IO box of the IOD domain to exclude the strong intrusion of the eastern equatorial cold tongue in the western IO simulated by the SINTEX model. See Sections 2.3 and 3.2 for details.

1089

1090

1091

1092

Table 1: Summary statistics for the first SST–USTR MCA leading mode (MCA1) applied onto 10°S–10°N monthly anomalies during boreal fall in the observations and the two experiments.

	SFC (%)	NC (%)	r inter-EC: SST – 20D	SSTvar (%)	20Dvar (%)	r EC – IOD Saji		r EC – IOD SINTEX	
						SST	20D	SST	20D
OBS	86.17	24.03	0.79	45.20	20.61	0.88	0.93	/	/
CTL	97.84	38.50	0.87	40.82	47.35	0.84	0.78	0.88	0.83
FTPC	95.41	34.57	0.85	35.26	46.45	0.77	0.71	0.84	0.78

1093

1094

Table 2: Same as Table 1 but for the SST–20D MCA1.

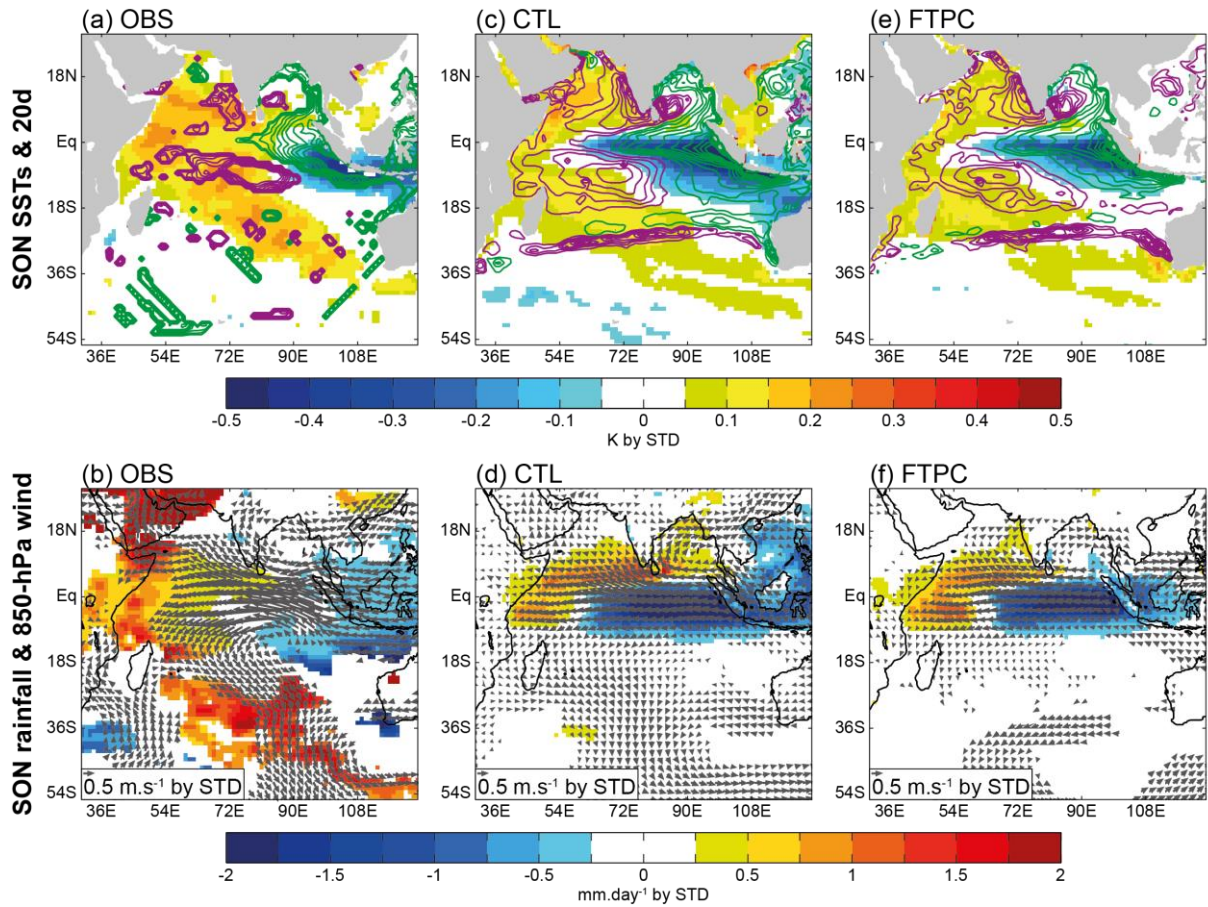
	SFC (%)	NC (%)	r inter-EC: 20D – USTR	20Dvar (%)	USTRvar (%)	r EC – IOD Saji		r EC – IOD SINTEX	
						20D	USTR	20D	USTR
OBS	88.01	24.08	0.80	21.72	41.31	0.91	0.86	/	/
CTL	95.65	30.13	0.77	47.28	32.19	0.78	0.77	0.83	0.82
FTPC	94.71	28.45	0.74	46.27	31.68	0.71	0.64	0.77	0.71

1095

1096

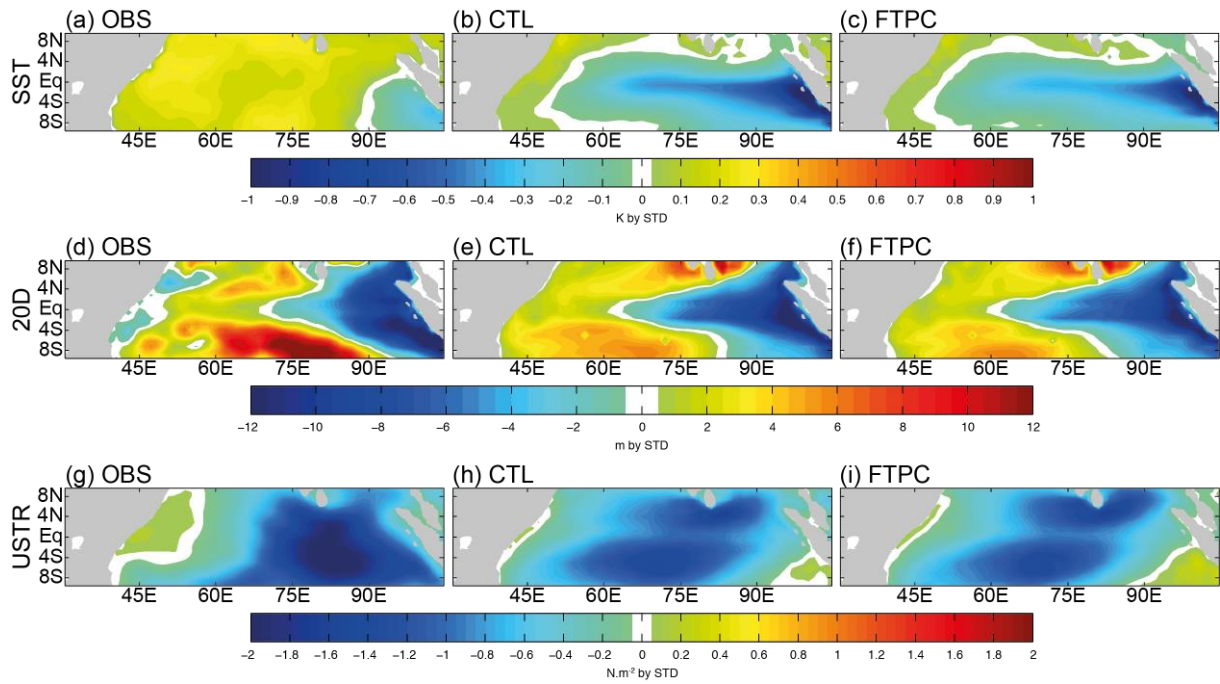
Table 3: Same as Table 1 but for the 20D–USTR MCA1.

1097 **Figures**
1098
1099



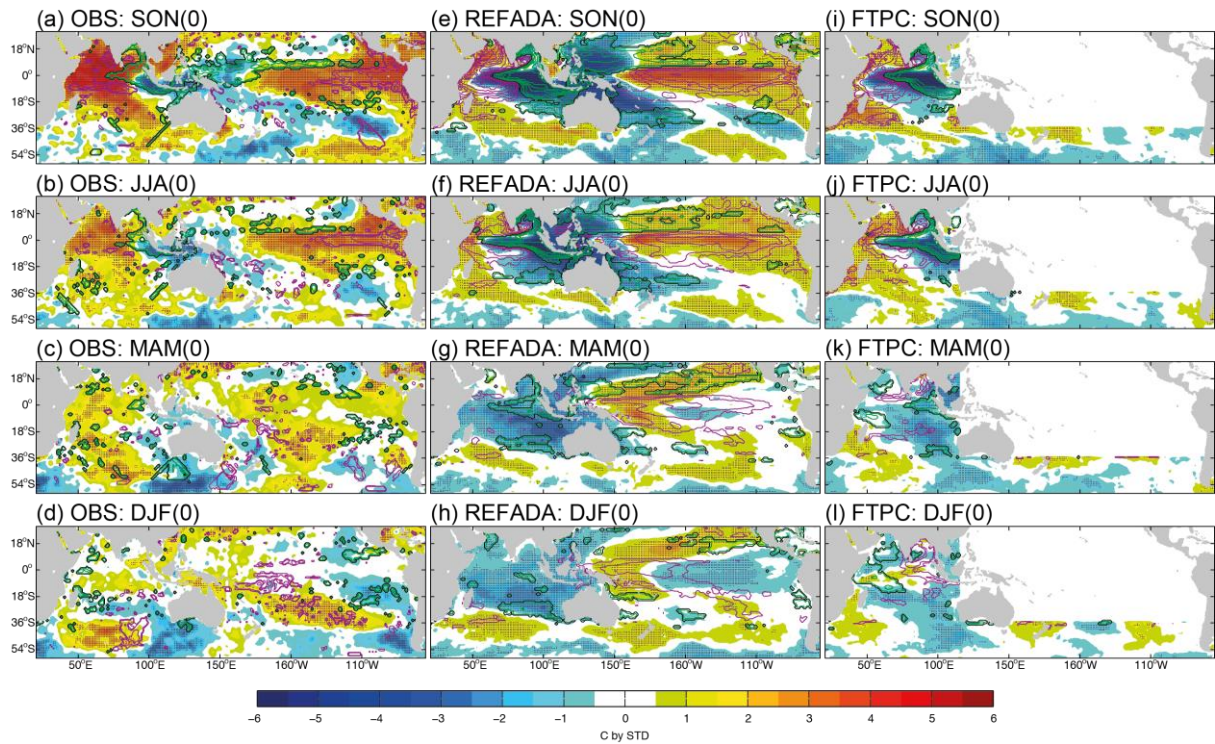
1100
1101
1102
1103
1104
1105
1106
1107
1108
1109
1110
1111

Figure 1: (a) September–November SST (shadings every 0.05 K) and 20°C isotherm depth (20D; contours every 1 m; green/purple contours for shallow/deep thermocline) anomalies regressed onto the normalized boreal fall (i.e., SON) IOD index from Saji et al. (1999) for the 1979–2008 observations. (b) Same as (a) but for rainfall (shadings every 0.25 mm.day⁻¹) and 850-hPa wind (vectors; m.s⁻¹) anomalies. (c–d) and (e–f) Same as (a–b) but for the CTL and the FTPC experiments, respectively. Anomalies that are not significant at the 90% confidence level according to a bootstrap test are masked. See Section 2.3 for details on the bootstrap test.



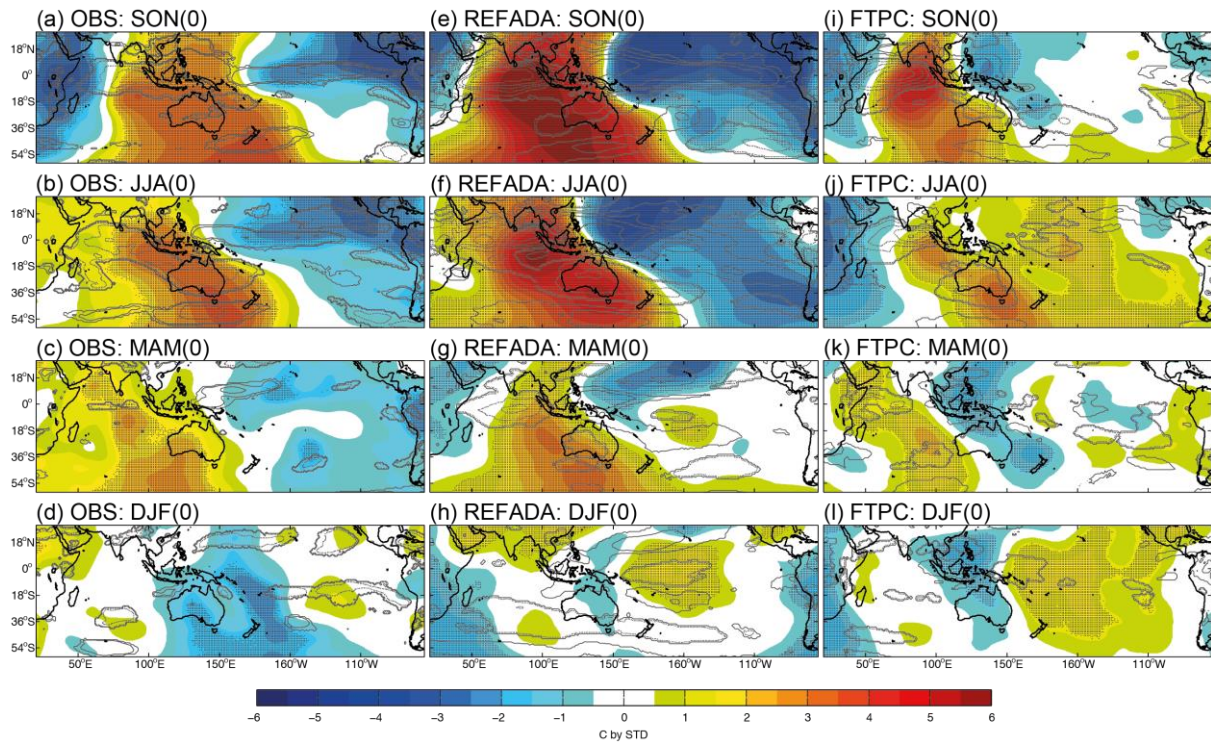
1112
 1113
 1114
 1115
 1116
 1117
 1118
 1119
 1120

Figure 2: (a) SST homogeneous map of the first leading MCA mode (MCA1) between monthly SST and 20D anomalies during boreal fall (September to November) for the 1979-2008 observations. (b-c) Same as (a) but for the CTL and FTPC experiments, respectively. (d-f) and (g-i) Same as (a-c) but for the 20D mode derived from the SST–20D MCA1 and for the USTR mode derived from the SST–USTR MCA1, respectively. Units are labeled on the Figure. Summary statistics for the different MCA1s are given in Tables 1-3.



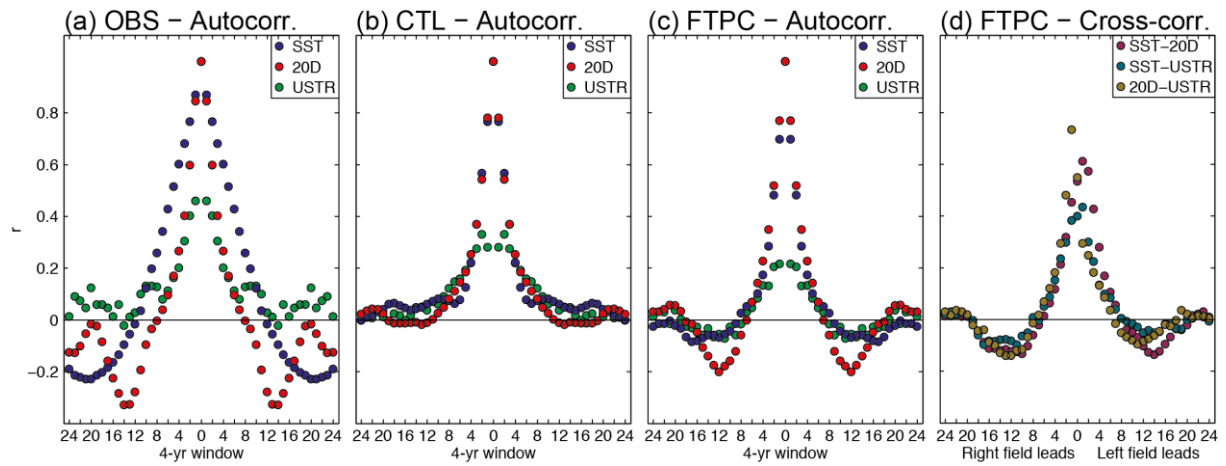
1121
 1122
 1123
 1124
 1125
 1126
 1127
 1128
 1129
 1130
 1131
 1132

Figure 3: (a-d) IOD prediction patterns of SST (shadings every 0.5 K) and 20D (contours every 1 K; green/purple contours for negative/positive coefficients and black contours for nullity) from the IOD peak season at year 0 (SON(0)) back to the preceding boreal winter (DJF(0)) for the observations. (e-h) and (i-l) Same as (a-d) but for the CTL and the FTFC, respectively. The IOD prediction patterns are obtained by regressing the non-normalized 20D EC time series derived from SST–20D MCA1 and averaged in SON(0) onto normalized quarterly anomalies at the grid point scale from SON(0) back to DJF(0). Significance tested at the 90% confidence level as in Fig. 1. Only significant IOD predictions are shown for 20D. Significant IOD predictions are shown with black dots for SST.



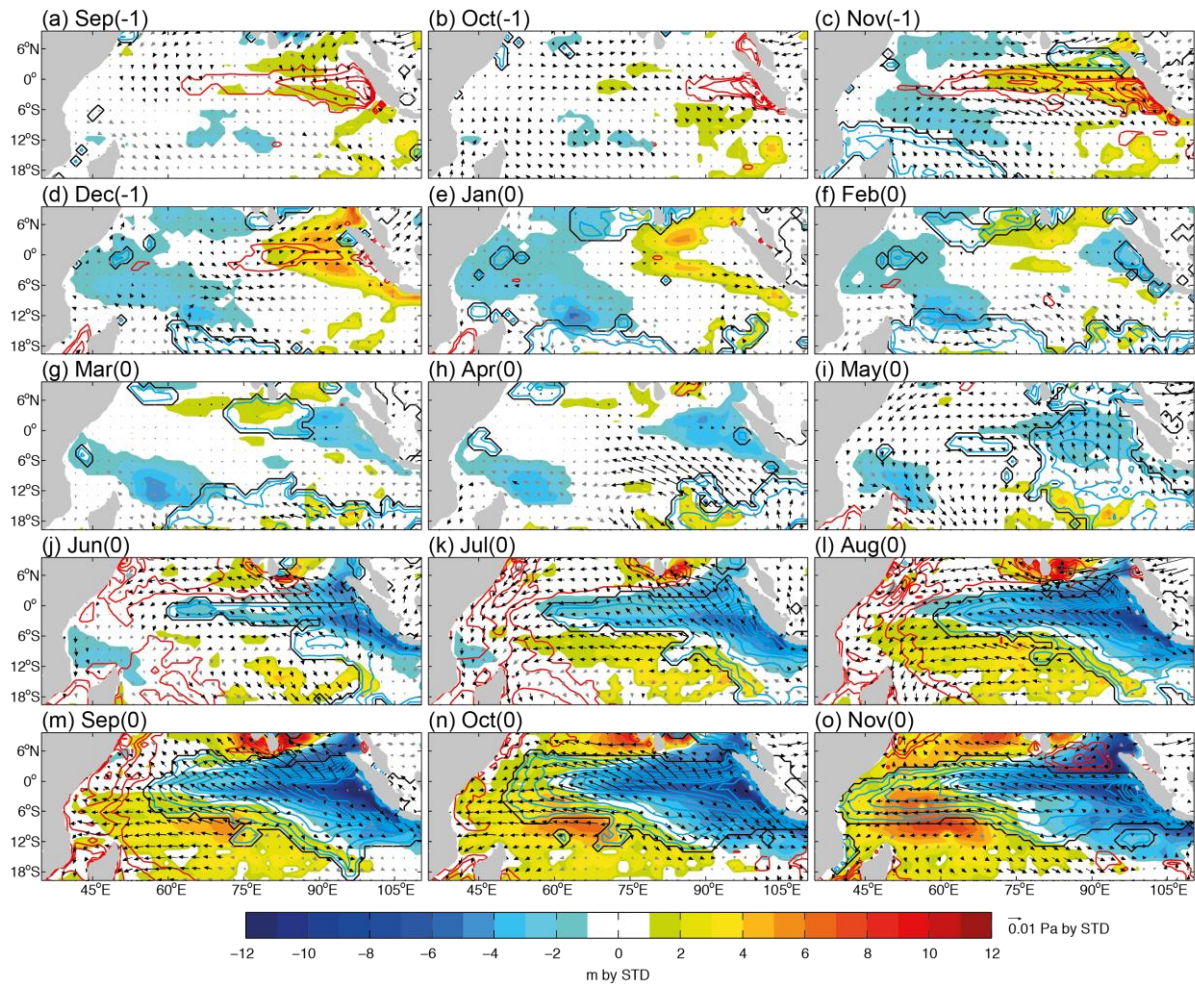
1133
 1134
 1135
 1136
 1137
 1138
 1139
 1140
 1141

Figure 4: Same as Fig. 3 but for the IOD prediction patterns derived from 200-hPa velocity potential (shadings every 0.5 K) and 850-hPa zonal wind (contours every 1 K; dotted/solid contours for negative/positive coefficients) anomalies. Only significant IOD predictions at the 90% confidence level are shown for 850-hPa zonal winds. IOD predictions significant at the 90% confidence level are shown with black dots for 200-hPa velocity potential.



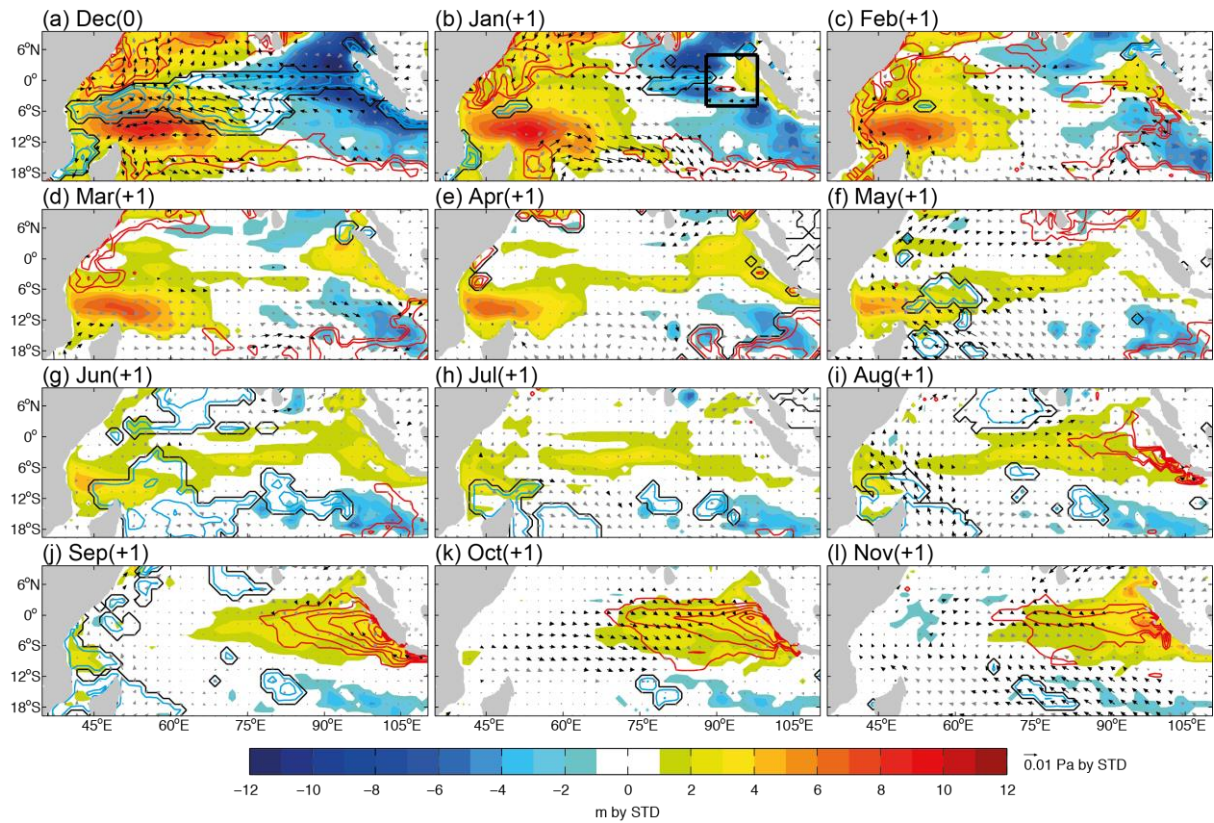
1142
1143

1144 **Figure 5:** (a) Autocorrelation in the monthly SST, 20D and USTR EC time series. (b-c)
 1145 Same as (a) but for the CTL and the FTPC, respectively. (d) Cross-correlation between the
 1146 three EC time series for the FTPC. The EC time series are computed by projecting the
 1147 monthly anomalies over the equatorial IO (10°S–10°N) for each variable onto the
 1148 corresponding singular vectors derived from SST–20D MCA1 for SST and 20D and from
 1149 SST–USTR MCA1 for USTR.



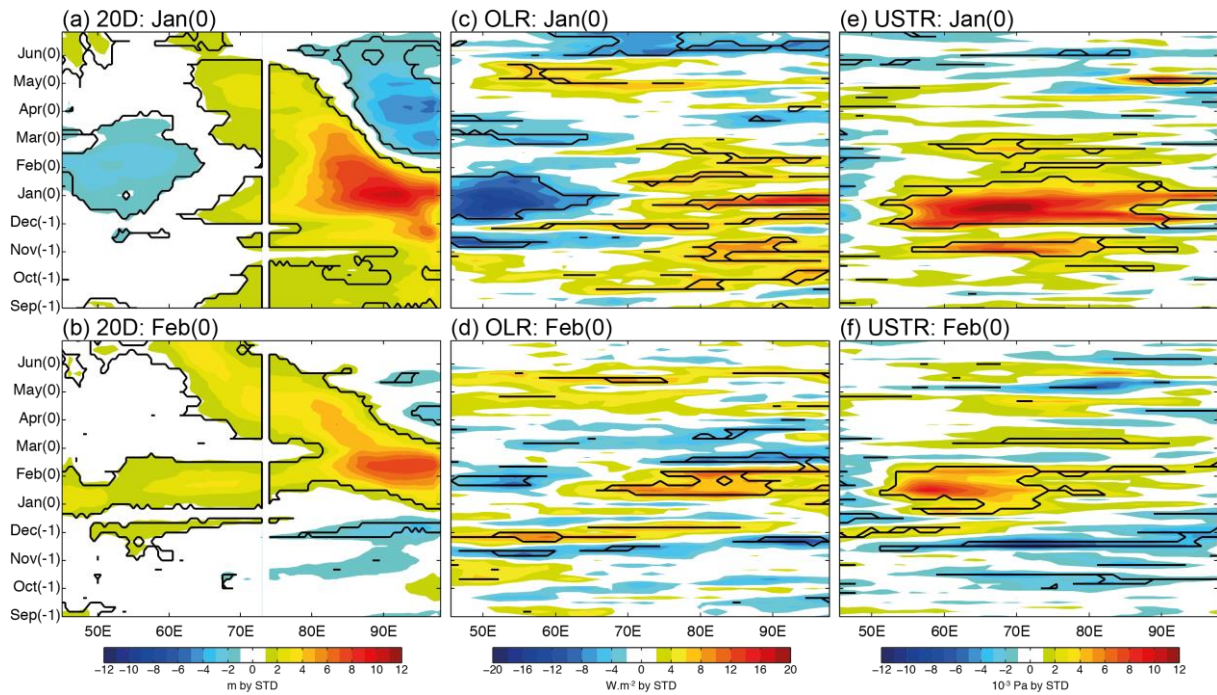
1150
 1151
 1152
 1153
 1154
 1155
 1156
 1157
 1158
 1159

Figure 6: Monthly SST (contours every 0.05 K; blue/red contours for SST cooling/warming and black contours for nullity), 20D (shadings every 1 K; cool/warm shadings for thermocline shoaling/deepening) and wind stress (vectors; Pascal) anomalies from (a) Sep(-1) to (o) Nov(0) regressed onto the normalized 20D EC time series from SST–20D MCA1 averaged during SON(0) for the FTPC experiment. Significance tested at the 90% confidence level as in Fig. 1. Only significant regression coefficients are shown for SST and 20D. Significant regression coefficients are shown by thick black arrows for wind stress.



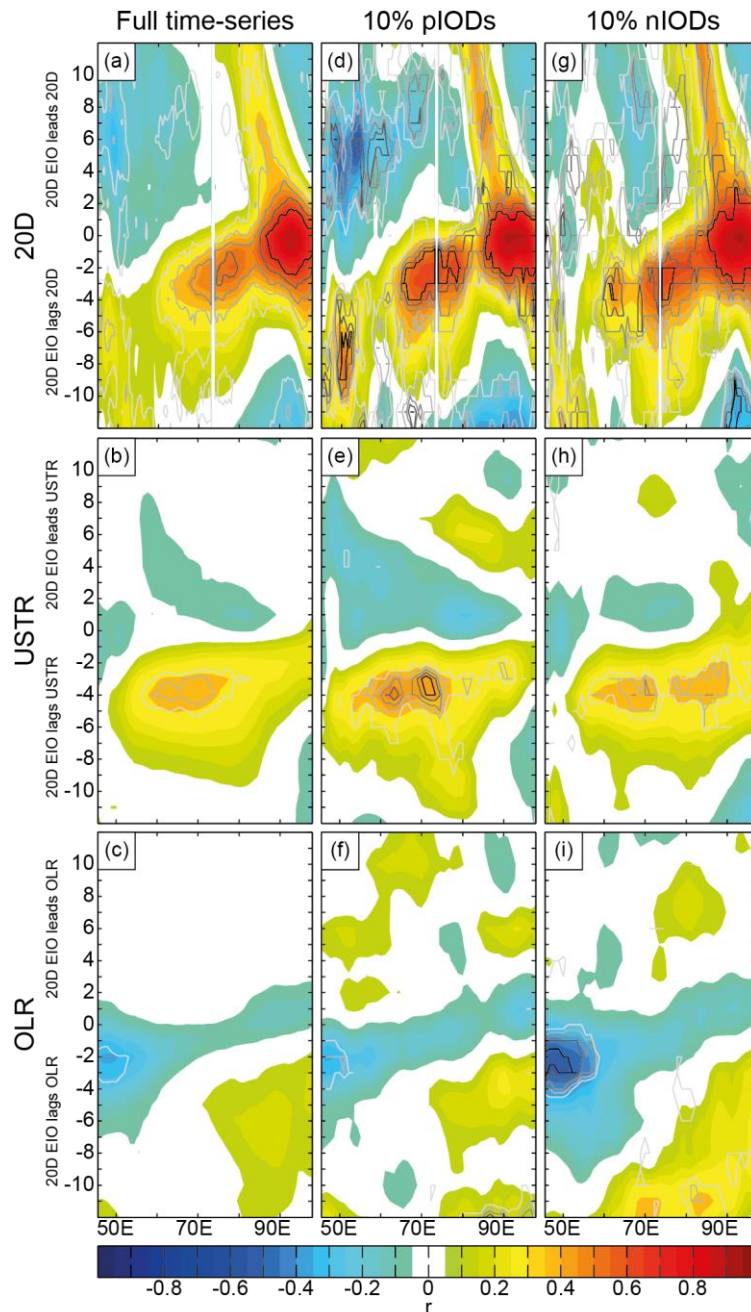
1160
 1161
 1162
 1163
 1164

Figure 7: Same as Fig. 6 but from (a) Dec(0) to (l) Nov(+1). The black box in panel b shows the domain used for computing the 20D index in Section 5.



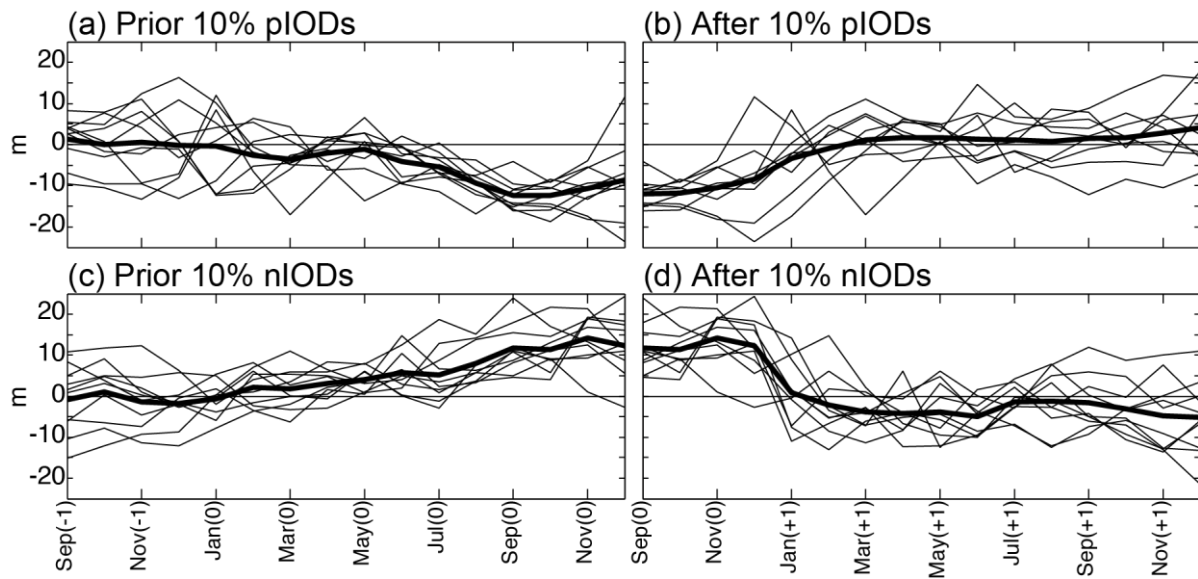
1165
 1166
 1167
 1168
 1169
 1170
 1171
 1172
 1173
 1174
 1175

Figure 8: (a) Regression of 5-day 20D anomalies area-averaged in the 2°S – 2°N band from September to June onto monthly 20D anomalies in the eastern equatorial IO (box shown in Fig. 7b) during January in the FTPC experiment. (b) Same as (a) but with the monthly 20D index in February. (c-d) and (e-f) Same as (a-b) but for 5-day OLR and USTR anomalies, respectively. Positive/Negative OLR and USTR anomalies correspond to weakened/strengthened convection and westerly/easterly wind anomalies, respectively. Black contours show significant regression coefficients at the 90% confidence level tested as in Fig. 1.



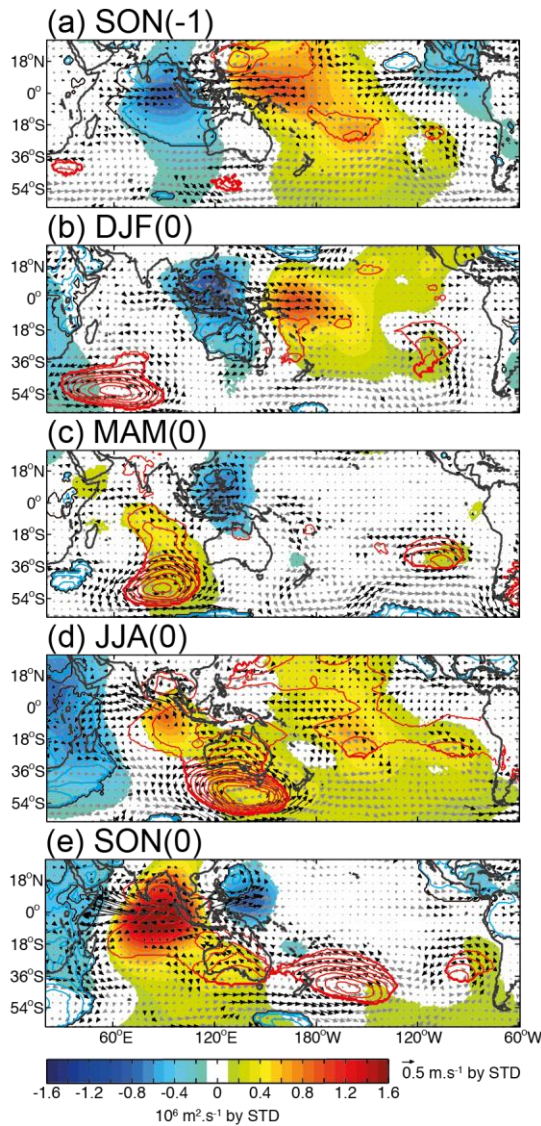
1176
 1177
 1178
 1179
 1180
 1181
 1182
 1183
 1184
 1185
 1186
 1187
 1188
 1189
 1190
 1191

Figure 9: Lead/lag pentad correlations between 20D anomalies area-averaged in the eastern equatorial IO (box in Fig. 7b) and zonal IO anomalies in (a-c) 20D, (d-f) USTR and (g-i) OLR averaged in the band 2°S-2°N for the FTPC experiment. Time series of both 20D index and climate zonal anomalies span 13 pentads. The 20D index is fixed and centered onto Dec 15, while climate zonal anomalies slide from 12 pentads ahead to 12 pentads after Dec 15, every 1 pentad. Lag 0 corresponds to the synchronous correlation (i.e., centered onto Dec 15). The direction of the lead/lag relationship is labeled on each panel. First, second and third columns correspond to lead/lag correlations averaged over the entire simulation period and for years following the 10% most intense pIODs and nIODs, respectively. The 10% most intense p/nIODs events are defined when the 20D EC time series (derived from SST-20D MCA1) averaged during SON is below/above its 10th/90th percentile threshold value. Significance is computed for each year at the 90% confidence level according to the Bravais-Pearson test. Light-to-dark contours show significant correlations reached 50% to 90% of the years, every 10%.



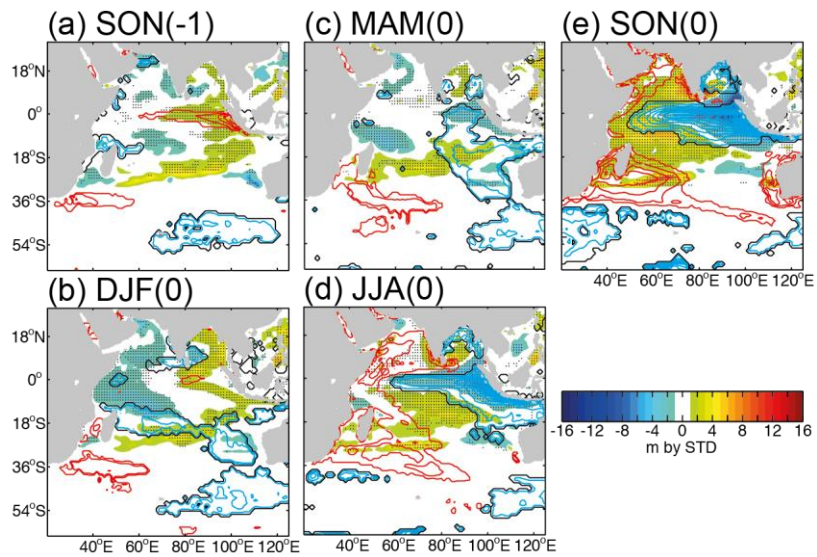
1192
 1193
 1194
 1195
 1196
 1197
 1198
 1199

Figure 10: (a-b) Monthly evolution of 20D anomalies (m), area-averaged in the eastern equatorial IO (box in Fig. 7b), one year back to the occurrence of pIODs and nIODs, respectively. (c-d) Same as (a-b) but one year after p/nIODs. Thin curves represent the 20D evolution of the 10% most intense IOD events (see Fig. 9 for definition) and thick curve is the ensemble mean.



1200
 1201
 1202
 1203
 1204
 1205
 1206
 1207
 1208
 1209
 1210

Figure 11: Regression of quarterly SLP (contours every 10 Pa, blue/red contour for low/high pressure and black contour for nullity), 200-hPa velocity potential (shadings every $1 \times 10^4 \text{ m}^2 \cdot \text{s}^{-1}$; cold/warm colors for upper-level divergence/convergence) and 850-hPa wind (vectors; $\text{m} \cdot \text{s}^{-1}$) anomalies regressed from (a) SON(-1) to (e) SON(0) onto the normalized 20D EC time series (derived from the SST-20D MCA1) in SON(0) for the FTPC experiment. Regression coefficients that are not significant at the 90% confidence level according to a bootstrap test are masked for SLP and 200-hPa velocity potential. Significant regression coefficients are shown by thick black arrows for 850-hPa wind.



1211
 1212
 1213
 1214
 1215
 1216
 1217

Figure 12: Same as Fig. 11 but for the regressions of 20D (shadings) and SST (contours) anomalies. Regression coefficients that are not significant at the 90% confidence level according to a bootstrap test are masked for SST. Significant 20D anomalies at the 90% confidence level are shown with black dots.